

TITLE

Transcription-mediated supercoiling regulates genome folding and loop formation

AUTHOR LIST AND AFFILIATIONS

**Maria Victoria Neguembor¹, Laura Martin^{1, 12}, Álvaro Castells-García^{1, 2, 12},
Pablo Aurelio Gómez-García¹, Chiara Vicario¹, Davide Carnevali¹, Jumana
AlHaj Abed³, Alba Granados¹, Ruben Sebastian-Perez¹, Francesco Sottile¹,
Jérôme Solon^{1, 4, 9, 10}, Chao-ting Wu^{3, 5}, Melike Lakadamyali^{6, 7, 13, *} and Maria
Pia Cosma^{1, 2, 4, 8, 11, 13, 14, *}**

¹ Centre for Genomic Regulation (CRG), The Barcelona Institute of Science and Technology, 08003 Barcelona, Spain.

² Bioland Laboratory, Guangzhou Regenerative Medicine and Health Guangdong Laboratory, Guangzhou 510005, China.

³ Department of Genetics, Harvard Medical School, Boston (Massachusetts), United States of America.

⁴ Universitat Pompeu Fabra (UPF), Dr Aiguader 88, 08003 Barcelona, Spain.

⁵ Wyss Institute for Biologically Inspired Engineering, Harvard University, Boston (Massachusetts), United States of America.

⁶ Perelman School of Medicine, Department of Physiology, University of Pennsylvania, 19104 Philadelphia (Pennsylvania), United States of America.

⁷ Perelman School of Medicine, Department of Cell and Developmental Biology, University of Pennsylvania, 19104 Philadelphia (Pennsylvania), United States of America.

⁸ ICREA, Pg. Lluís Companys 23, 08010 Barcelona, Spain.

⁹ Instituto Biofisika (CSIC, UPV/EHU), Basque Excellence Research Centre, Barrio Sarriena, 48940, Leioa, Spain.

¹⁰ Ikerbasque, Basque Foundation for Science, 48013 Bilbao, Spain.

¹¹ CAS Key Laboratory of Regenerative Biology, Guangdong Provincial Key Laboratory of Stem Cell and Regenerative Medicine, Guangzhou Institutes of Biomedicine and Health, Chinese Academy of Sciences, Guangzhou 510530, China

¹² These authors contributed equally.

¹³ Senior authors.

¹⁴ Lead contact

* Corresponding authors: pia.cosma@crg.es (M.P.C.) and melikel@pennmedicine.upenn.edu (M.L.).

SUMMARY

The chromatin fiber folds into loops, however the mechanisms controlling loop extrusion are still poorly understood. Using super-resolution microscopy, we visualize that loops in intact nuclei are formed by a scaffold of cohesin complexes from which the DNA protrudes. RNA polymerase II decorates the top of the loops and is physically segregated from cohesin. Augmented looping upon increased loading of cohesin on chromosomes causes disruption of Lamin at the nuclear rim and *chromatin blending*, a homogenous distribution of chromatin within the nucleus. Altering supercoiling via either transcription or topoisomerase inhibition counteracts chromatin blending, increases chromatin condensation, disrupts loop formation and leads to altered cohesin distribution and mobility on chromatin. Overall, negative supercoiling generated by transcription is an important regulator of loop formation *in vivo*.

INTRODUCTION

A key to understanding life is dissecting how the genome is folded within the nucleus and how 3-D genomic organization regulates gene activity (Lakadamyali and Cosma, 2020). Yet, our knowledge of the mechanisms controlling genome organization is still limited. In particular, while it is established that genome organization regulates gene transcription, it is largely underexplored whether transcription, in turn, shapes genomic organization.

Recently, methods of chromosome conformation capture (3C, Hi-C, ChIA-PET among others) allowed the detection of genomic regions in physical proximity, revealing *cis* and *trans* contacts at multiple genomic scales, from chromatin compartments to Topological Associated Domains (TADs) and chromatin loops (Dixon et al., 2012; McCord et al., 2020; Nora et al., 2012; Sexton et al., 2012). Loops and TAD boundaries are enriched with the CCCTC-binding factor (CTCF) and the cohesin complex (Dixon et al., 2012; Nativio et al., 2009; Nora et al., 2012; Parelho et al., 2008; Rao et al., 2014; Vietri Rudan et al., 2015; Wendt et al., 2008).

Loops are thought to represent a key structure in controlling gene expression by mediating direct contacts between gene regulatory elements (Rao et al., 2014).

Interestingly, loops are dynamic, constantly growing and undergoing remodelling (Hansen et al., 2017; Rao et al., 2017). A model that explains loop formation, based on extrusion of loops by the cohesin complex, was suggested as early as 2001 (Nasmyth, 2001). Currently, the most accepted view of how loops are generated postulates that they are created upon entrapment of the chromatin fiber by cohesin. The DNA forming the loops is processively extruded until cohesin is arrested by the presence of stalling factors, such as CTCF, or by cohesin unloading (Fudenberg et al., 2016; Hassler et al., 2018; Rowley and Corces, 2018; Sanborn et al., 2015; van Steensel and Furlong, 2019). Proteins involved in the loading and unloading of cohesin, NIPBL/MAU2 and WAPL/PSD5 respectively (Kueng et al., 2006; Sutani et al., 2009; Watrin et al., 2006), were shown to control loop size (Haarhuis et al., 2017; Schwarzer et al., 2017; Wutz et al., 2017).

Recently it has been shown that cohesin complexes use ATPase activity to translocate autonomously through the DNA fiber. In line with this idea, cohesin has been shown to extrude loops *in vitro* in the presence of ATP and NIPBL/MAU2 (Davidson et al., 2019; Kim et al., 2019). While this loop extrusion activity needs to be confirmed *in vivo*, additional questions remain regarding the validity of a model exclusively driven by motor activity dependent extrusion. For example, how is the directionality of extrusion controlled and sustained? Transcriptional machinery was proposed to directly drive loop extrusion by physically pushing cohesin along DNA through the processive motion of RNA polymerase II (RNAP II) (Busslinger et al., 2017; Davidson et al., 2016; Ocampo-Hafalla et al., 2016; Stigler et al., 2016; Tran et al., 2017; Wang et al., 2017). However, given that RNAP II is estimated to proceed at a speed of up to 90 bp/sec, while the speed of loop formation has been estimated between 374 and 850 bp/sec (Rowley and Corces, 2018), how can RNAP II be sufficiently fast to sustain the speed of loop formation?

To reconcile these open questions, we here investigated whether transcription indirectly controls loop extrusion, through transcription-derived negative

supercoiling. Negative supercoiling is generated as a by-product of transcription and produces high amounts of free energy that could power cohesin sliding through chromatin in an oriented manner (Racko et al., 2018, 2019). Supercoiling has been proposed to mediate the formation of underwound and overwound domains genome-wide and computational modelling predicts that supercoiling may help in driving the formation of TADs and loops by generating torsional tension that pushes cohesin along the DNA (Benedetti et al., 2014; Naughton et al., 2013; Racko et al., 2018, 2019; Ruskova and Racko, 2021). While this is an attractive hypothesis, there is no direct evidence supporting that transcription-derived supercoiling could control loop extrusion and cohesin function.

The recent development of super-resolution microscopy provides exciting opportunities in the field of genome architecture, allowing the study of chromatin organization at multiple levels (Beliveau et al., 2015; Bintu et al., 2018; Boettiger et al., 2016; Cardozo Gizzi et al., 2019; Mateo et al., 2019; Nguyen et al., 2020; Nir et al., 2018; Ricci et al., 2015; Su et al., 2020). We thus took advantage of a variety of Single Molecule Localization Microscopy (SMLM) approaches, including Stochastic Optical Reconstruction Microscopy (STORM), OligoSTORM, DNA points accumulation for imaging in nanoscale topography (DNA-PAINT) and Single Molecule Tracking (SMT), to investigate the possible key role of transcription in genome organization and loop formation. We provide support for transcription-dependent negative supercoiling to be a driving factor of loop extrusion by cohesin *in vivo*.

RESULTS

Vermicelli are formed by a core of multiple cohesin clusters, and RNAP II preferentially accumulates at their edges

We investigated in detail the structure of cohesin mediated DNA-loops by carrying out two-color STORM/DNA-PAINT imaging of DNA and the cohesin subunit SMC1A, in serum starved WAPL Δ HeLa cells (Figure S1A, B). WAPL-deficient cells accumulate high amounts of cohesin on chromosomes and exhibit a worm-like

organization of cohesin called *vermicelli* (Tedeschi et al., 2013). Vermicelli are generated by increased rates of loop extrusion (Busslinger et al., 2017; Haarhuis et al., 2017; Kueng et al., 2006), thus allowing the dissection of loop structure. To impair WAPL activity, as previously reported (Rhodes et al., 2017a), we targeted M1116, an essential residue of WAPL (Figure S1C, D). By inspecting the spatial arrangement of SMC1A and DNA in vermicelli at different orientations in WAPL Δ cells, we observed that cohesin clusters located in close proximity align to form the longitudinal axis of the vermicelli around which DNA is wrapped and protrudes (Figure 1A). Cohesin complexes form a scaffold at the heart of vermicelli and generate a footprint (Figure 1A, white asterisks) from which DNA filaments are extruded (Figure 1A, yellow arrows).

Using a previously developed cluster identification algorithm (Ricci et al., 2015), we analyzed SMC1A STORM images to compare the size of SMC1A clusters localized in vermicelli against the size of SMC1A clusters in the nucleus or in the cytosol of control cells (Figure S1E). We assumed that cytosolic clusters are composed of individual SMC1A proteins and appear as clusters in STORM images due to the amplification of the signal resulting from antibody labeling and repeated fluorophore blinking (Zanacchi et al., 2017). By normalizing the number of localizations in the nuclear clusters of SMC1A to the average number of localizations in the cytosolic clusters, we obtained an estimate of the number of cohesins forming both the nuclear clusters in control cells and the clusters within vermicelli of WAPL Δ cells. In control cells, clusters of SMC1A in nuclei contained on average 1.5 SMC1A proteins per cluster and had 3.1 ± 0.59 fold larger area than cytosolic clusters (Figure 1B, C, S1E). In WAPL Δ cells, clusters within vermicelli contained 2.6 SMC1A proteins per cluster and had 4.2 ± 1 fold larger area than cytosolic clusters (Figure 1B, C, S1E). Interestingly, the clusters of SMC1A in WAPL Δ nuclei residing outside vermicelli were similar in size to cytosolic clusters, likely representing single nuclear cohesins (Figure 1B, C, S1E). These results agree with the model that vermicelli structures are formed by long loops generated by progressive loop extrusion from multiple cohesins that collide with neighboring ones (Haarhuis et al.,

2017; Tedeschi et al., 2013; Wutz et al., 2017). Hence, cohesin clusters present in the axial core of the vermicelli are likely to be the bases of extruded loops.

Since RNAP II has been hypothesized to be an important regulator of loop extrusion (Busslinger et al., 2017; Davidson et al., 2016; Ocampo-Hafalla et al., 2016; Racko et al., 2018, 2019; Stigler et al., 2016; Tran et al., 2017; Vian et al., 2018; Wang et al., 2017), we then investigated how RNAP II is distributed with respect to the loops. In WAPL Δ cells we performed 3-D STORM for DNA and RNAP II combined with diffraction-limited imaging of SMC1A to identify the vermicelli. Examining vermicelli in axial and longitudinal orientations revealed that RNAP II is excluded from the core scaffold structure of vermicelli, where cohesin accumulates, and preferentially locates at the edges of vermicelli, which correspond with low density DNA (Figure 1D, E and Movie 1). Pearson correlation analysis of colocalization of confocal images of DNA, RNAPII and SMC1A further supports this finding. Correlation coefficients are higher for DNA-SMC1A than for DNA-RNAP II (Figure S1F and Movie 1). Additionally, in *wt* HeLa cells nearest neighbour distance (NND) analysis of dual-color super-resolution images of RNAP II and SMC1A showed that RNAP II and cohesin were not physically associated (Figure S1G-I).

Blocking transcriptional activity triggers chromatin compaction and impairs cohesin distribution and mobility on chromatin

Our data showed that RNAP II locates at the edge of the loops, physically decoupled from cohesin. To conclusively test if RNAP II plays any role in controlling loop extrusion as previously hypothesized (Busslinger et al., 2017; Davidson et al., 2016; Ocampo-Hafalla et al., 2016; Racko et al., 2018, 2019; Stigler et al., 2016; Tran et al., 2017; Vian et al., 2018; Wang et al., 2017), we sought to determine whether the inhibition of RNAP II would impact the spatial organization of DNA or cohesin distribution and function. To inhibit transcription, we used drugs that inhibit RNAP II with different modes of action: 5,6-dichloro-1- β -D ribofuranosylbenzimidazole (DRB), Flavopiridol, Triptolide and α -Amanitin (Figure S2A-D). We found that the coefficient of variation (CV) of the DNA signal, thus the

DNA compaction, increased in confocal images, indicating increased heterogeneity in the distribution of DNA in treated cells compared to more uniformly distributed DNA in controls. Notably, the effect on DNA compaction was reversible, after treatment with the reversible drug DRB (Figure S2A, B). We then confirmed the progressively increased CV using Actinomycin D (ActD), another transcriptional inhibitor, for different treatment times (Figure S2E-G). Of note, when cells were treated with the intercalating drug Hoechst that does not inhibit RNAP II, CV was comparable to controls (Figure S2H, I), excluding trivial effects related to the intercalation on the DNA fiber. These data suggest an increase in DNA compaction, which was consistent among several different RNAP II inhibitors. Hence, we decided to use ActD to study the influence of transcription on DNA organization and cohesin at the nanoscale level.

Next, we investigated in depth the organization of DNA upon transcriptional inhibition with super-resolution microscopy. STORM images of DNA showed a marked increase of densely packed chromatin in ActD-treated cells, which was quantitatively confirmed by Voronoi tessellation analysis (Andronov et al., 2016; Levet et al., 2015; Otterstrom et al., 2019), and an increase in DNA-free nuclear area relative to control cells (Figure 2A-C). Treatment with the intercalating drug Hoechst did not lead to DNA compaction as quantified by Voronoi tessellation analysis of DNA STORM images (Figure 2D). We then used OligoSTORM (Beliveau et al., 2015; Beliveau et al., 2012; Boettiger et al., 2016) to image at nanoscale level two pairs of contiguous genes in IMR90 human primary fibroblasts: *GAPDH-IFFO1* genes, which were transcriptionally active, and *OCT4-TCF19*, which were repressed (Figure S2J). Following ActD treatment, *GAPDH-IFFO1* became repressed as expected (Figure S2K). Voronoi tessellation analysis of OligoSTORM data showed increased localization density as compared to the more dispersed localization distribution in control cells (Figure 2E, F) as well as a reduced radius of gyration (Figure 2G), indicating increased compaction. On the other hand, transcriptionally repressed *OCT4-TCF19* genes (Figure S2J) displayed a highly-compacted conformation in controls, and this was unchanged upon ActD treatment (Figure 2H-J), suggesting that heterochromatin regions do not undergo hyper-

condensation upon transcription inhibition. These results further support that transcriptional inhibition increases DNA compaction, and this effect is more prominent for transcriptionally active genes.

ActD is known to inhibit both RNAP I and II (Perry and Kelley, 1970), we thus blocked RNAP I using CX5461 and did not observe any detectable DNA compaction, confirming that the changes were due to the activity of RNAP II (Figure S3A, B). Finally, to rule out any other side effects of drug treatments, we used mAID-mClover-RPB1 DLD1 cells to deplete RNAP II via proteolytic degradation (Nagashima et al., 2019). Degradation of RNAP II phenocopied the impact of transcriptional inhibitors, leading to significant DNA compaction and confirming the specificity of our findings (Figure S3C, D). Overall, STORM revealed that inhibiting RNAP II does affect the spatial organization of DNA, leading to global chromatin compaction.

To determine if these changes in DNA compaction and spatial organization were due to impairment in loop extrusion by cohesin, we then investigated the impact of RNAP II inhibition on cohesin distribution and function. Upon transcriptional inhibition we observed a decrease in the level of co-localization of DNA and of SMC1A (Figure 3A, B). Importantly, H3K9me3, a hallmark of heterochromatin, and Enhancer of Zeste 2 (EZH2), a histone methyltransferase catalytic component of the Polycomb Repressive Complex 2, remain fully associated with chromatin after ActD treatment (Figure 3C, D, S3E, F), thereby excluding that the co-localization analysis was biased by differences in the spatial organization of DNA and validating its accuracy.

To further investigate the impact of transcription on cohesin distribution and activity, we studied the dynamics of RAD21. As expected RAD21 and SMC1A, being stoichiometric subunits of the same complex, co-localize with DNA to the same extent (Figure S3G) and form clusters of comparable size, i.e. area and the number of localizations per cluster (Figure S3H, I). We then performed single molecule tracking (SMT) of RAD21 in living U2OS cells where both *RAD21* alleles were tagged with HaloTag (Rhodes et al., 2017b). H3.3, tagged with SNAP showed that

ActD treatment lead to chromatin compaction in U2OS cells similar to our observations in HeLa cells, suggesting that the effects of transcriptional inhibition are cell-type independent (Figure S3J). SMT experiments in living cells showed longer residence times of the cohesin complexes bound to chromatin in ActD-treated cells compared to controls (Figure 3E). Additionally, we found reduced radius of confinement of the chromatin-bound cohesin after ActD treatment (Figure 3F). Taken together SMT analysis and STORM imaging indicate that the distribution and mobility of cohesin on the chromatin fiber are affected when transcription is inhibited; the co-localization of cohesin with DNA decreased and the remaining cohesin complexes display longer dwell time and reduced mobility.

The reduced mobility of cohesin led us to hypothesize that the translocation and extrusion activity of cohesin might be impaired. If this is indeed the case, cohesin should be stalled at sites of loading or along genes if RNAP II is no longer active. H3K4me2 is enriched at active transcription start sites (TSS), where cohesin is thought to be preferentially loaded by NIPBL and generally it associates to active genes (Table S1) (Busslinger et al., 2017; Kagey et al., 2010; Zuin et al., 2014). Thus, we co-imaged SMC1A and H3K4me2 in DMSO-treated and ActD-treated cells. NND and cross pair correlation analyses showed increased association between SMC1A and H3K4me2 in ActD-treated cells as compared both to control cells and to a simulation of randomly-distributed protein clusters at the same density (Figure 3G-I, S4A). Similar experiments and analyses showed no change in the association between SMC1 and SMC3, which are equimolar within cohesin rings (Figure S4B-E). Likewise, the proximity between SMC1A and H3K27me3, which is not enriched at active TSS or at transcribed regions, did not increase upon ActD treatment, ruling out that proximity changes between SMC1A and H3K4me2 could simply be due to chromatin compaction upon transcriptional inhibition (Figure S4F-H).

Overall, our results show that inhibition of RNAP II reduces cohesin mobility. Cohesin increases co-localization with H3K4me2, suggesting a possible accumulation at active TSS as well as along transcribed genes. These results

hence support a role for RNAP II mediated transcription in regulating cohesin function and translocation along chromosomes.

Inhibition of transcription blocks chromatin blending caused by the excess of loop extrusion

Having established that transcription profoundly affects DNA compaction and cohesin mobility and distribution along DNA in wild type cells, we aimed to study if inhibition of RNAP II would affect DNA compaction and spatial distribution of cohesin in WAPL-deficient cells (Figure 4A). We first analyzed the baseline DNA distribution in WAPL Δ cells in which RNAP II was not inhibited. Interestingly, super-resolution images revealed a homogeneous distribution of DNA across the nucleus compared to controls, with strongly reduced segregation of low- and highly-compacted chromatin. This DNA distribution is observed in the density rendering in heatmaps and the quantitative Voronoi analysis of STORM imaging (Figure 4B upper panels and 4C). We named the distribution of DNA in WAPL Δ cells “chromatin blending”. Further, we observed that the heterochromatin marked by H3K9me3 exhibited reduced accumulation at the nuclear periphery and redistribution to the nuclear interior in WAPL Δ cells (Figure 4D and S4I, J). These observations along with chromatin blending suggest that upon excess of cohesin loading eu- and hetero-chromatin are spatially mixed. Given these results, we next asked how the Lamin A/C was affected in WAPL Δ cells. In WAPL Δ , we observed disruption of the fibrillar organization of Lamin A/C at the nuclear rim, the accumulation of clustered Lamin in the nucleoplasm (Figure 4E, F) and decreased DNA density at the nuclear rim (Figure 4E). This result agrees with data showing fragmentation of Lamin Associated Domains (LADs) in WAPL Δ cells, previously shown by DNA adenine methyltransferase identification (DamID) experiments (Haarhuis et al., 2017). Our findings suggest that an excess of loop extrusion can potentially pull LADs towards the nuclear interior, thereby disrupting Lamin architecture and promoting compartment mixing. Consistent with our results, in WAPL-depleted cells, together with fragmentation of LADs, a preferential switch

from B to A compartments and decreased segregation between compartments have been observed (Busslinger et al., 2017; Haarhuis et al., 2017; Nuebler et al., 2018). We then tested whether inhibition of RNAP II could affect the eu- and hetero-chromatin mixing of WAPL Δ cells. Interestingly, when WAPL Δ or control cells were treated with ActD (Figure 4A), the inhibition of transcription fully abrogated DNA blending and reverted the phenotype to chromatin compaction, thus having a dominant effect over WAPL mutation (Figure 4B lower panels and 4C).

Inhibiting transcription blocks the formation of vermicelli

Given the dominant effect of transcription inhibition on DNA spatial organization over WAPL mutation, we asked whether the global organization of cohesin in the form of vermicelli in WAPL Δ cells could be affected by the block of transcription. Inhibition of RNAP II caused a remarkable reorganization of cohesin, resulting in the disruption of vermicelli (Figure 5A). Upon ActD treatment, the number of WAPL Δ cells containing vermicelli was strongly reduced (Figure 5B and S5A), which was also the case in isolated cell clones (Figure S1D and S5B). Likewise, treatment with Flavopiridol, Triptolide and DRB lead to a significant decrease of vermicelli nuclei in WAPL Δ cells (Figure S5C). Also, we generated WAPL Δ DLD1 cells. Upon IAA treatment, RNAP II depleted cells showed a significant decrease of vermicelli nuclei (Figure S5D). On the contrary, vermicelli were insensitive to the RNAP I inhibitor, CX5461 (Figure S5E) and to the intercalating drug Hoechst (Figure S5F), further supporting the specific role of RNAP II in altering cohesin topology.

The reorganization of cohesin upon transcriptional inhibition was further confirmed by Voronoi tessellation followed by threshold-based segmentation, under the different treatment conditions (Figure S5G). This analysis allowed the identification and quantification of isolated cohesin clusters as well as vermicelli structures consisting of multiple cohesin clusters aligned in close proximity (Figure S5G). In the DMSO-treated WAPL Δ cells the size of the vermicelli structures (i.e. mean area and mean number of localizations per vermicelli) was significantly higher than the

isolated cohesin clusters in control and ActD-treated cells, further confirming that vermicelli structures are disrupted by RNAP II inhibition (Figure 5C, D and S5G).

To discern if vermicelli disassembly upon RNAP II inhibition was due to altered cohesin activity rather than to the reduction of cohesin abundance on the chromatin fiber, we partially reduced cohesin levels by lentiviral transduction of shRNAs against *SMC1A* and *SMC3* subunits (Figure S6A-C). Compared to cells transduced with non-silencing (NS) shRNA controls, knockdown of both *SMC1A* and *SMC3* led to partial DNA decompaction as revealed by DNA STORM and Voronoi tessellation analysis (Figure 5E, F). Importantly, the WAPL mutation in *SMC3*-knockdown cells triggered the formation of vermicelli structures at levels comparable to NS controls (Figure 5G and S6D). Thus, under normal transcriptional activity, partial loss of cohesin is not sufficient *per se* to trigger DNA compaction or loss of vermicelli. However, ActD treatment of WAPL Δ cells following knockdown of *SMC3* reduced the percentage of vermicelli to control levels (Figure 5G and S6D). Collectively, these data show that disruption of cohesin vermicelli is not simply due to decreased abundance of cohesin but rather to the effect of transcriptional inhibition on cohesin mobility and distribution.

Taken together, our data show that inhibition of transcription abolishes chromatin blending and the formation of vermicelli in WAPL Δ cells. These results further demonstrate that transcriptional activity and RNAP II are required for proper cohesin function.

Given our results showing that transcription affects cohesin function, we asked whether loop domains include transcribed regions across the genome. By intersecting the coordinates of loop domains from Hi-C and Micro-C datasets (Krietenstein et al., 2020; Rao et al., 2014) with the coordinates of coding genes we found a significant enrichment of expressed genes within loop domains across the seven cell types examined (Fisher's exact test, Table S2). Specifically, up to 87.7% of loops contained active genes (Table S3) and, strikingly, up to 43 % of loops contained genes belonging to the highest expression fraction (top 25 % most expressed genes of the corresponding cell type; Table S3), further suggesting the relation between transcription and loop domains.

Transcription-derived supercoiling and topoisomerase activity control loop formation

Previous works reported an overlap between topological boundaries, loop domains and supercoiling, thereby it has been suggested that supercoiling levels are correlated to loop domain structures (Naughton et al., 2013; Rao et al., 2014). Moreover, molecular dynamics simulations predicted that negative supercoiling could be a driving force for cohesin loop extrusion and could mediate the formation of TADs (Benedetti et al., 2014; Racko et al., 2018, 2019). Specifically, it has been predicted that plectonemic structures generated by transcription create net free energy sufficient to push cohesin along the chromosomes, away from transcribed regions (Gilbert and Allan, 2014). As cohesin complexes embrace the chromatin fiber tightly, they can slow the dissipation of the torsional stress, maintaining high levels of negative supercoiling. Finally, supercoiling is released when cohesin complexes reach TAD borders that are enriched for Topoisomerase 2 (Top2) (Canela et al., 2017; Gothe et al., 2019; Racko et al., 2018, 2019; Uuskula-Reimand et al., 2016), which alleviates the torsional tension. Top2 inhibition leads to an accumulation of positive supercoiling and knots (Fernandez et al., 2014; Joshi et al., 2012; Valdes et al., 2019; Valdes et al., 2018), which results in a net decrease of negative supercoiling. Likewise, Topoisomerases 1 (Top1) regulates the level of supercoiling in eukaryotic cells (Bjorkegren and Baranello, 2018; Pommier et al., 2010; Pommier et al., 2016). Top1 localizes at the front of RNAP II and preferentially relaxes positive supercoiling, leading to a net increase of negative supercoiling, which allows transcription (Baranello et al., 2016; Fernandez et al., 2014). Therefore, after inhibiting Top1, one would expect a reduction of negative supercoiling.

Motivated by previous work and our observations, we reasoned that an excess of cohesin could interfere with supercoiling dissipation, so we asked if WAPL Δ cells showed altered levels of supercoiling. We therefore imaged WAPL Δ and control cells that had incorporated biotinylated trimethylpsoralen (bTMP) to probe the

levels of DNA negative supercoiling (Bermudez et al., 2010; Ljungman and Hanawalt, 1992, 1995; Naughton et al., 2013; Sinden et al., 1980). WAPL Δ cells showed greater bTMP signals than controls, indicating higher levels of negative supercoiling (Figure 6A and S7A). As previously reported *in vitro* for the bacterial looping mediating factor Lac I (Yan et al., 2018), here we infer that cohesin limits the dissipation of torsional tension of DNA in WAPL Δ cells, which accumulate negative supercoiling forming longer loops than control cells. Thus, our results suggest that in WAPL Δ cells negative supercoiling cannot be efficiently resolved and therefore increases.

To further investigate the role of transcriptionally-derived supercoiling and the contribution of fiber torsional tension on genome organization and loop formation, we inhibited Top1 and Top2 with b-lapachone and Doxorubicin, respectively. We reasoned that inhibiting topoisomerase activities, thus perturbing the supercoiling state of the fiber, should recapitulate the effects of transcriptional inhibition. Using confocal imaging and quantification of the DNA CV, we found that b-lapachone and doxorubicin triggered DNA compaction (Figure S7B, C). DNA STORM imaging and Voronoi tessellation analysis confirmed this observation (Figure 7B-D). As observed for ActD treatment and relative to controls, b-lapachone treatment led to decreased overlap of SMC1A and DNA, showing altered cohesin distribution on DNA (Figure 7E, F).

Next, we asked whether topoisomerase inhibition could affect vermicelli formation, we treated WAPL Δ cells with b-lapachone and Doxorubicin. Both topoisomerase inhibitors significantly decreased the percentage of nuclei displaying vermicelli, similar to ActD treatment (Figure 6G, S7D, E). These results further support that aberrant supercoiling impairs cohesin activity and looping likely due to altered torsional stress of the fiber. Lastly, to confirm this observation, we determined that inhibition of both transcription and topoisomerase comparably affects the levels of DNA supercoiling in control and WAPL Δ cells. For this we performed bTMP incorporation and imaging quantification in ActD-, Flavopiridol- and b-lapachone-treated cells. Upon treatment, control and WAPL Δ cells displayed decreased levels

of bTMP incorporation indicating decreased accumulation of negative supercoiling, thereby even counteracting the formation of long loops (Figure S7F). These results indicate that transcription and topoisomerase activities cooperate, likely by altering torsional tension in the fiber, regulating the level of supercoiling to control cohesin activity and loop formation (Figure 7).

DISCUSSION

Over the last few years both super-resolution microscopy and Hi-C technologies showed that 3-D spatial organization of the interphase chromosomes has profound consequences for the transcriptional activity of the genome (Bintu et al., 2018; Cardozo Gizzi et al., 2019; Lakadamyali and Cosma, 2020; McCord et al., 2020; Nir et al., 2018; Su et al., 2020). In parallel, growing experimental and modelling data carried out in a variety of organisms suggest that transcription itself can shape genome architecture and might have a role in loop extrusion (Barutcu et al., 2019; Busslinger et al., 2017; Davidson et al., 2016; Grubert et al., 2020; Hug et al., 2017; Le et al., 2013; Lengronne et al., 2004; Li et al., 2015; Ocampo-Hafalla et al., 2016; Olan et al., 2019; Racko et al., 2018, 2019; Rowley et al., 2019; Stigler et al., 2016; Tran et al., 2017; Vian et al., 2018; Wang et al., 2017).

Using advanced SMLM techniques, we studied in single cells at unprecedented resolution the cross-talk between transcription and cohesin and how this cross-talk shapes the genome structure in interphase cells. Previous work showed that cohesin is three times more abundant in the transcriptionally active A compartment than in the B compartment (Schwarzer et al., 2017), and it has been suggested that increased transcriptional activity might favour cohesin loading (Gassler et al., 2017; Kagey et al., 2010). Here, we provide direct evidence that transcription regulates cohesin, since blocking transcription alters cohesin distribution on DNA and cohesin mobility (Busslinger et al., 2017; Kagey et al., 2010; Zuin et al., 2014). Overall, our results indicate that transcriptional activity regulates the movement/translocation of cohesin along chromatin. Most importantly, in WAPL Δ cells inhibition of RNAP II abolishes chromatin blending and the formation of

vermicelli-structured chromosomes. Previous work, which reported chromatin compaction upon α -Amanitin or Flavopiridol treatments, also suggest that transcription regulates chromatin organization (Naughton et al., 2013; Vian et al., 2018) and ActD inhibition was shown to decrease TAD boundaries (Barutcu et al., 2019). Notably, recent work revealed that transcription could rewire loops at specific genes, showing that transcription-dependent *de novo* cohesin peaks disappear upon transcriptional inhibition with DRB (Olan et al., 2019). Here, we show that preserving cohesin dynamics, rather than its abundance, is key to maintaining the organization of the genome and cohesin mediated loops. In summary, we show that transcription promotes cohesin activity on chromatin and that inhibition of transcription results in chromatin compaction and impaired cohesin function.

Super-resolution microscopy revealed that the increased level of loop extrusion in WAPL Δ cells generates chromatin blending, Lamin A/C dissociation from the nuclear edge, and relocation of H3K9me3-marked heterochromatin from the nuclear periphery to the nuclear interior. Collectively, these phenotypes likely reflect an altered segregation of heterochromatin and euchromatin. Accordingly, previous Hi-C experiments estimated that longer loops identified in WAPL Δ and PSD5 Δ cells correlate with decreased segregation of A and B compartments and preferential compartmental switch from B to A (Haarhuis et al., 2017; Wutz et al., 2017). Our observation of the loss of the Lamin A/C fibrillar structure at the nuclear periphery let us to speculate that the blending of DNA, i.e. excess of looping, could pull heterochromatin regions towards the nuclear interior. It will be interesting in the future to evaluate the impact this phenomenon has on the possible activation of heterochromatic regions and how looping affects the interaction between chromatin and subnuclear structures. Overall, our findings about DNA blending and the global reorganization of chromatin support the growing evidence that loop extrusion is an opposing force to phase separation in defining hetero- and euchromatin compartments (Gassler et al., 2017; Haarhuis et al., 2017; Hilbert et al., 2021; Nuebler et al., 2018; Rowley et al., 2019).

Transcription and supercoiling are intimately related. Transcription generates torsional stress at both sides of the transcription bubble and topoisomerases are essential to relieve this torsional stress to allow transcriptional elongation (Pommier et al., 2016). Additionally, maintaining basal levels of negative supercoiling at promoters is essential to ensure transcriptional initiation (Pommier et al., 2016). Therefore, the tight control of the topological state of the chromatin fiber by topoisomerases is key to sustain transcription. The potential link between supercoiling and global genome organization has gradually emerged, especially in bacteria and lower eukaryotes (Gilbert and Allan, 2014; Marinov et al., 2020). Recently, cohesin has been proposed to play an important role in this picture, as cohesin could contribute to control genome topology by confining and channelling torsional stress (Orlandini et al., 2019). Accordingly, loop anchors and TAD boundaries are enriched for topoisomerases (Canela et al., 2019; Canela et al., 2017; Gothe et al., 2019; Uuskula-Reimand et al., 2016). In agreement with previous evidence, we show that blocking topoisomerases phenocopies transcriptional inhibition. Top1 and Top2 inhibition led to global chromatin compaction, decreased overlap of cohesin with DNA and reduced formation of vermicelli. Furthermore, inhibition of topoisomerase and transcription decreased negative supercoiling in WAPL Δ cells where the excess of cohesin decreases the efficiency of supercoiling dissipation thus leading to longer loops. This finding, together with the observation that RNAP II accumulates at the edge of the loops, physically decoupled from cohesin, led us to conclude that transcription acts on cohesin activity through transcription-derived supercoiling.

The genome is pervasively transcribed and even heterochromatin has a basal level of transcription (Djebali et al., 2012; Hangauer et al., 2013; Saksouk et al., 2015), which can generate supercoiling. Supercoiling can propagate through tens or hundreds of kilobases (Kramer et al., 1999; Kramer and Sinden, 1997; Matsumoto and Hirose, 2004; Naughton et al., 2013; Postow et al., 2004). Although in one study the maximum level of supercoiling was seen at TSS (Kouzine et al., 2013), this does not exclude that multiple rounds of abortive transcription or frequent transcription over short stretches of DNA, such as enhancer RNAs, could in

principle introduce multiple waves of supercoiling boosting the torsional state of a region far away from the protein-coding genes (Arner et al., 2015; Kim et al., 2010; Kim et al., 2015; Racko et al., 2018).

Increasing experimental evidence strongly indicates that the establishment of genome organization is not governed by a single control mechanism but rather by a combination of synergistic and antagonistic factors (McCord et al., 2020; Nuebler et al., 2018; Rowley and Corces, 2018; van Steensel and Furlong, 2019). Recent studies have shown that the ATPase activity of cohesin mediates loop extrusion *in vitro* (Davidson et al., 2019; Kim et al., 2019). In addition, ATP was shown to be essential to establish loop domains (Vian et al., 2018). Thus, cohesin-mediated extrusion and supercoiling-mediated extrusion could act as complementary forces regulating cohesin distribution.

In conclusion, super resolution microscopy allowed us to visualize DNA loops, and determine that transcription-mediated supercoiling shapes genome architecture and has a key role in loop extrusion by controlling cohesin activity. In the next years, the combination of super-resolution imaging approaches with genomic methods will fully unveil how the cross talk between transcription and 3-D genome organization controls gene and cell function (Lakadamyali and Cosma, 2020).

Limitations of the Study

In the absence of a unifying principle governing genome folding, transcription- and supercoiling-mediated control of cohesin can be contributing factors. Moreover, although we excluded that DNA intercalation *per se* has an effect on loop formation, it might also be that structural alterations of DNA folding can have an additive contributing effect. We cannot exclude that transcription impacts genome organization in additional ways and that alternative mechanisms promote folding at non-transcribed regions. For instance, RNA itself was shown to promote compartment segregation and recruitment of CTCF to chromatin (Barutcu et al., 2019; Saldana-Meyer et al., 2019). However, while nuclear RNA was reported to influence compartment segregation and CTCF function, it did not affect TAD

boundary formation, which was instead influenced by transcription activity and was CTCF independent (Barutcu et al., 2019). We thus speculate that the impact of transcription on cohesin that we demonstrate here is independent of the impact of transcription on CTCF activity. We cannot exclude however that transcription-induced supercoiling in cooperation with the effect of RNA transcripts on CTCF have a combined activity on genome folding, an interesting topic for further investigation in the future.

ACKNOWLEDGMENTS

The authors acknowledge Peter Hitchcock (University of Michigan) and Eric F. Joyce (UPENN) for critical reading of the manuscript. The authors acknowledge Nick Gilbert (University of Edinburgh, UK), Bo Huang (UCSF, USA), Luke Lavis (Janelia Research Campus, USA), Kim Nasmyth (University of Oxford, UK), Kazuhiro Maeshima (National Institute of Genetics, Japan) and Feng Zhang (Broad Institute, USA) for kindly sharing bTMP reagent, Insight3 software, JF dyes, SNAP-H3.3 + SCC1-Halo U2OS cells, mAID-mClover-POLR2A DLD-1 cells and pSpCas9(BB)-2A-GFP (pX458) plasmid. The authors acknowledge the advanced light microscopy (ALMU), the genomics and the FACS units from CRG for their excellent technical support. The authors acknowledge the support from European Union's Horizon 2020 Research and Innovation Programme [CellViewer No 686637 to J.S., M.L., M.P.C.]; Ministerio de Ciencia e Innovación, grant [BFU2017-86760-P (AEI/FEDER, UE) to M.P.C.], and an AGAUR grant from Secretaria d'Universitats i Recerca del Departament d'Empresa i Coneixement de la Generalitat de Catalunya [(2017 SGR 689) to M.P.C.]; Centro de Excelencia Severo Ochoa [2013–2017 to M.P.C.]; CERCA Programme/Generalitat de Catalunya [to M.P.C.]; the Spanish Ministry of Science and Innovation to the EMBL partnership [to M.P.C.]; National Natural Science Foundation of China [31971177 to M.P.C.]; Innovative Team Program of Guangzhou Regenerative Medicine and Health Guangdong Laboratory [2018GZR110103001 to M.P.C.]; Linda Pechenik Montague Investigator Award [to M.L.]; University of Pennsylvania Epigenetics Pilot Award [to M.L.]; the Center for Engineering and Mechanobiology (CEMB) an NSF Science and Technology Center

Pilot Award [CMMI: 15-48571 to M.L.]; NIH grants R01HD091797 and R01GM123289 [to C.t.W.]; People Program (Marie Curie Actions) FP7/2007–2013 under REA grant [608959 to M.V.N.]; Juan de la Cierva-Incorporación 2017 [to M.V.N.]; Grant for the recruitment of early-stage research staff FI-2020 [Operational Program of Catalonia 2014-2020 CCI 2014ES05SFOP007 of the European Social Fund to L.M.]; "La Caixa" Foundation Fellowship (ID 100010434, #LCF/BQ/DR20/11790016) [to L.M.]; "La Caixa-Severo Ochoa" pre-doctoral fellowship [to A.C.G.]; Secretaria d'Universitats i Recerca del Departament d'Empresa i Coneixement de la Generalitat de Catalunya and the co-finance of Fondo Social Europeo [2018FI_B_00637 and FSE to R.S.P.], La Caixa international PhD fellowship [to F.S.].

AUTHOR CONTRIBUTIONS

Conceptualization, M.V.N. and M.P.C.; Methodology, M.V.N., L.M., A.C.G., C.V. and P.A.G.G.; Software, C.V., P.A.G.G. and A.G.; Formal analysis: M.V.N., L.M., A.C.G., C.V., D.C., A.G. and P.A.G.G.; Investigation, M.V.N., L.M., A.C.G., R.S.P., F.S.; Visualization, M.V.N., L.M., A.C.G., C.V. and P.A.G.G.; Writing –Original Draft, M.V.N., M.L. and M.P.C.; Writing –Review & Editing, A.C.G., L.M., C.V., P.A.G.G., J.A.A., A.G., R.S.P., F.S., J.S. and C.t.W.; Funding Acquisition, J.S., M.L. and M.P.C.; Resources, J.A.A. and C.t.W.; Supervision, C.t.W., J.S., M.L. and M.P.C.

DECLARATION OF INTERESTS

C.t.W. holds or has patent filings pertaining to Oligopaints and related technologies, including other oligo-based methods for imaging. Her laboratory also has active collaborations with industry for the development of Oligopaint technologies and holds a sponsored research agreement with Bruker Inc. She is also a non-equity holding co-founder and member of the scientific advisory board of Acuity Spatial Genomics, and, through personal connections to George Church, has equity in companies associated with him (<http://arep.med.harvard.edu/gmc/tech.html/>), including 10x Genomics and Twist.

INCLUSION AND DIVERSITY

We worked to ensure diversity in experimental samples through the selection of the cell lines. One or more of the authors of this paper self-identifies as living with a disability.

MAIN FIGURE TITLES AND LEGENDS

Figure 1. The organization of loops revealed in WAPL Δ cells

- A. Super-resolution (SR) images of DNA (EdC-AF647 labeling, magenta) and SMC1A (DNA-PAINT immunolabeling, green) in WAPL Δ cells. Zoom in longitudinal view of a vermicelli. Yellow arrows: DNA extruding from SMC1A clusters. White asterisks: SMC1A positions within vermicelli.
 - B. Normalized mean number of SMC1A per cluster in Control Cytosol, Control Nuclei, WAPL Δ Nuclei Vermicelli, and WAPL Δ Nuclei out Vermicelli (n = 10 cytosolic areas, and 35, 20 and 19 nuclei respectively). Values are normalized by Control Cytosol average value. Mean and standard deviation (SD); Kruskal-Wallis test with Dunn's correction for multiple comparisons, ** p = 0.0075 and 0.0059, **** p < 0.0001, ns > 0.9999.
 - C. Normalized mean area of clusters of SMC1A in Control Cytosol, Control Nuclei, WAPL Δ Nuclei Vermicelli, and WAPL Δ Nuclei out Vermicelli (n = 10 cytosolic areas, and 35, 20 and 19 nuclei respectively). Values are normalized by Control Cytosol average value. Mean and SD; Kruskal-Wallis test with Dunn's correction for multiple comparisons, * p = 0.0314, **** p < 0.0001, ns p > 0.9999.
 - D. 3D SR images of DNA (magenta) and RNAP II phSer2 (green), and conventional image of SMC1A (cyan) in WAPL Δ cells.
 - E. Zoom in examples of vermicelli from D in axial (i) and longitudinal orientation (ii); (iii) Axial cut of longitudinal vermicelli, DNA (white) and RNA Pol II phSer2 (color-coded in z).
- See also Figure S1 and Movie 1.

Figure 2. Inhibition of transcription triggers global and locus specific DNA compaction

- A. Heatmap density rendering of super-resolution images of DNA (EdC-AF647 labeling) in Control (DMSO) and Actinomycin D (ActD) treated HeLa cells. Full nuclei (left panels) and zoomed views (right panels) are shown.

- B. Percentage of DNA-free area per nucleus quantified from super-resolution images of EdC-AF647 labeled DNA in DMSO and ActD-treated HeLa cells, $n = 21$ and 19 nuclei respectively. Mean and SD; unpaired two-tailed t test, **** $p < 0.0001$.
- C. Cumulative distribution of Voronoi polygons' densities of DNA in DMSO (purple) and ActD-treated (green) cells ($n = 21$ and 19 nuclei respectively). Median (thick line) and standard error of the mean values (SEM) (shaded area, which is not visible due to low values of the standard error: 1.745 for DMSO and 1.188 for ActD); unpaired two-tailed t test, **** $p < 0.0001$.
- D. Cumulative distribution of Voronoi polygons' densities of DNA in H₂O (purple) and Hoechst-treated (pink) cells ($n = 17$ and 15 nuclei respectively). Median (thick line) and standard error of the mean values (SEM) (shaded area, which is not visible due to low values of the standard error: 2.331 for H₂O and 2.793 for Hoechst); unpaired two-tailed t test, ns $p = 0.0881$.
- E. OligoSTORM images of *GAPDH-IFFO1* gene locus (24.5 kb) in IMR90 fibroblasts in Control (DMSO) and ActD-treated IMR90 fibroblasts. Gaussian rendering (magenta) and heatmap density rendering (color scale) of super-resolution imaging of the locus.
- F. Cumulative distribution of Voronoi polygons' densities of OligoSTORM *GAPDH-IFFO1* locus (24.5 kb) in DMSO ($n = 38$ loci) and ActD-treated cells ($n = 36$ loci). Median and SEM; two-tailed Mann-Whitney test, ** $p = 0.0047$.
- G. Radius of gyration quantification of *GAPDH-IFFO1* OligoSTORM loci (24.5 kb) in DMSO- and ActD-treated cells ($n = 47$ and 40 loci respectively). Mean and SD; two-tailed Mann-Whitney test, * $p = 0.0331$.
- H. OligoSTORM images of *OCT4-TCF19* gene locus (78 kb) in IMR90 fibroblasts in Control (DMSO) and ActD-treated IMR90 fibroblasts. Gaussian rendering (magenta) and heatmap density rendering (color scale) of super-resolution imaging of the locus.
- I. Cumulative distribution of Voronoi polygons' densities of OligoSTORM *OCT4-TCF19* loci (78 kb) in DMSO ($n = 30$ loci) and ActD-treated cells ($n = 30$ loci). Median and SEM; two-tailed Mann-Whitney test, ns $p = 0.5422$.

- J. Radius of gyration quantification of *OCT4-TCF19* loci (78 kb) in DMSO (n = 31 loci) and ActD (n = 30 loci). Mean and SD; two-tailed Mann-Whitney test, ns p = 0.3622.

See also Figure S2.

Figure 3. Inhibition of transcription affects cohesin distribution and mobility

- A. SR images of DNA (magenta) and SMC1A (green) in DMSO and ActD-treated HeLa cells.
- B. Colocalization index of SMC1A with DNA in DMSO and ActD in individual nuclei (n = 17 nuclei each). Mean and SD; unpaired two-tailed t test, **** p < 0.0001.
- C. Super-resolution images of DNA (EdC-AF647 labeling, in magenta) and H3K9me3 (DNA-PAINT immunolabeling, in green) in Control (DMSO) and ActD-treated HeLa cells. Full nuclei (left panels) and zoomed views (right panels) are shown.
- D. Colocalization index of H3K9me3 with DNA in DMSO and ActD-treated cells (n = 8 and 9 nuclei respectively). Mean and SD; unpaired two-tailed t test, ns p = 0.8802.
- E. Residence times in seconds of RAD21 molecules determined by SMT in DMSO and ActD-treated U2OS. N = 9230 and 4715 tracks, respectively. Mean and 95% CI; unpaired two-tailed t test, **** p < 0.0001.
- F. Radius of confinement in nanometers of RAD21 molecules determined by SMT in DMSO and ActD-treated U2OS cells, n = 1284 and 446 confined tracks, with 89162 and 27206 jumps, respectively. Mean and 95% CI; unpaired two-tailed t test, **** p < 0.0001.
- G. Dual-color super-resolution images of SMC1A (magenta) and H3K4me2 (green) in DMSO and ActD-treated HeLa cells. Representative zoomed nuclear areas are shown.
- H. Nearest Neighbor Distance (NND) distribution plot of the distance between H3K4me2 and SMC1A clusters in DMSO and ActD-treated HeLa cells; n =

31 and 24 nuclei respectively. Experimental data are shown as continuous lines, random simulated data are displayed as dotted lines.

- I. Nearest Neighbor Distance (NND) distribution between H3K4me2 and SMC1A clusters in DMSO (purple) and ActD (green) HeLa cells. Values corresponding to the difference between experimental and random simulated data are plotted.

See also Figure S3 and Table S1.

Figure 4. WAPL Δ cells display chromatin blending and altered Lamin A/C organization

- A. Schematic representation of experimental workflow.
- B. Heatmap density rendering of super-resolution images of DNA (EdC-AF647 labeling) in Control and WAPL Δ HeLa cells upon DMSO (upper panels) and ActD (lower panels) treatment. Right panels display zoom in views of the nuclear regions indicated with squares of the corresponding colors.
- C. Cumulative distribution of the Voronoi polygon densities of DNA in DMSO, WAPL Δ DMSO, ActD and WAPL Δ ActD cells (n = 12, 8, 9 and 9 nuclei respectively). Median (thick line) and SEM (shaded area); one-way ANOVA with Tukey's test for multiple comparisons, **** p < 0.0001.
- D. Percentage of H3K9me3 at nuclear edges quantified in Controls (n = 21) and WAPL Δ cells (n = 21 and 14 nuclei respectively). Mean and SD; unpaired two-tailed t test, **** p < 0.0001.
- E. SR images of DNA (magenta) and Lamin A/C (green) in Controls and WAPL Δ cells. Right panels display zoom in views of the nuclear regions indicated with white squares.
- F. Percentage of Lamin A/C at nuclear edges quantified in Controls and WAPL Δ cells (n = 7 nuclei each). Mean and SD; unpaired two-tailed t test, *** p = 0.0008.

See also Figure S4.

Figure 5. Inhibition of transcription counteracts chromatin blending and blocks the formation of vermicelli

- A. SR images of DNA (magenta) and SMC1A (green) in WAPL Δ cells upon DMSO and ActD.
- B. Percentage of vermicelli nuclei per experiment in WAPL Δ cell populations, $n = 6$ independent experiments. Mean and SD; two-tailed Mann-Whitney test, ** $p = 0.0022$.
- C. Mean number of localizations per Voronoi cluster of SMC1A in DMSO, WAPL Δ DMSO, ActD and WAPL Δ ActD cells ($n = 32, 19, 28$ and 28 nuclei respectively). Mean and SD; one-way ANOVA with Tukey's test for multiple comparisons, **** $p < 0.0001$.
- D. Mean area of Voronoi clusters of SMC1A in DMSO, WAPL Δ DMSO, ActD and WAPL Δ ActD cells ($n = 32, 19, 28$ and 28 nuclei respectively). Mean and SD; one-way ANOVA with Tukey's test for multiple comparisons, **** $p < 0.0001$.
- E. Heatmap density rendering of SR images of DNA (EdC-AF647) in Control shRNA (NS), *SMC1A* kd and *SMC3* kd HeLa cells.
- F. Cumulative distribution of the Voronoi polygon densities of DNA in NS, *SMC1A* kd and *SMC3* kd cells ($n = 17, 14$ and 15 nuclei respectively). Median (thick line) and SEM (shaded area); one-way ANOVA with Tukey's test for multiple comparisons, * $p = 0.0122$ and **** $p < 0.0001$.
- G. Percentage of cells with vermicelli per field in DMSO and ActD treated WAPL Δ NS and WAPL Δ *SMC3* kd cells, $n \geq 10$ fields. Mean and SD; Kruskal-Wallis test with Dunn's correction for multiple comparisons, *** $p = 0.0001$, ** $p = 0.0011$ and ns $p > 0.9999$.

See also Figures S5 and S6 and Tables S2 and S3.

Figure 6. Topoisomerase inhibition triggers DNA compaction and counteracts vermicelli formation in WAPL Δ cells

- A. Mean Fluorescence intensity in arbitrary units (Streptavidin-AF488) of b-TMP treated control and WAPL Δ cells and of mock controls to test negative

supercoiling levels. Mean and SD, $n \geq 52$ nuclei; two-tailed Mann-Whitney test, **** $p < 0.0001$.

- B. Heatmap density rendering of SR images of DNA (EdC-AF647) in DMSO, b-lapachone (b-Lap) and Doxorubicin (Doxo) treated (5h) HeLa cells.
- C. Percentage of DNA-free area per nucleus quantified from SR images of DNA in DMSO, b-Lap and Doxo-treated (5h) HeLa cells, $n = 15, 14$ and 16 nuclei respectively. Mean and SD; one-way ANOVA with Tukey's test for multiple comparisons, **** $p < 0.0001$.
- D. Cumulative distribution of Voronoi polygons' densities of DNA in DMSO, b-Lap and Doxo-treated (5h) cells ($n = 16, 14$ and 16 nuclei respectively). Median (thick line) and SEM (shaded area, which is not visible due to low values of the standard error: 2.646 DMSO, 1.952 b-Lap and 1.631 Doxo); two-tailed Mann-Whitney test, **** $p < 0.0001$.
- E. SR images of DNA (magenta) and SMC1A (green) in DMSO and b-Lap-treated HeLa cells.
- F. Colocalization index of SMC1A with DNA in DMSO and b-Lap (5h) in individual nuclei ($n = 12$ and 10 nuclei respectively). Mean and SD; unpaired two-tailed t test, **** $p < 0.0001$.
- G. Percentage of cells with vermicelli per experiment in DMSO and b-Lap- and Doxo-treated (5h) WAPL Δ cell populations, $n \geq 4$ independent experiments. Mean and SD; unpaired two-tailed t test, ** $p = 0.0010$ and *** $p = 0.0009$. See also Figure S7.

Figure 7. Proposed model.

Schematic cartoon depicting how inhibition of topoisomerases and of RNAP II leads to global chromatin compaction and decreased levels of negative supercoiling, thereby impairing cohesin activity and loop extrusion. Chromatin (in blue) displays segregation and balance between euchromatin and heterochromatin in *wt* cells, while chromatin blending and increased negative supercoiling is observed in WAPL Δ cells. Cohesin (in magenta) is enriched at the base of the loops while RNAP II (in green) is preferentially found at the edges of the extruded DNA loops.

STAR METHODS

RESOURCE AVAILABILITY

Lead contact

Further information and requests for resources and reagents should be directed to and will be fulfilled by the Lead Contact: Maria Pia Cosma (pia.cosma@crg.es).

Materials availability

All unique/stable reagents generated in this study are available from the Lead Contact with a completed Materials Transfer Agreement.

Data and code availability

RNA-seq and ChIP-seq datasets are deposited under accession number (GSE169492). Data for imaging and western blot figures in the paper is available (Mendeley Data - DOI: 10.17632/pbnc4zhc wd.1). Other datasets and custom-made scripts used in this work are available upon request.

EXPERIMENTAL MODEL AND SUBJECT DETAILS

Cell lines used and culture conditions

HeLa, IMR90 (ATCC, #CCL-186) and RAD21-Halotag SNAP-H3.3 U2OS (Rhodes et al., 2017b), all female cells, were cultured in Dulbecco's Modified Eagle Medium (DMEM, Thermo Fisher Scientific, #41965039) supplemented with 10% Fetal Bovine Serum (FBS, Thermo Fisher Scientific, #10270106), 1% Penicillin-Streptomycin (Thermo Fisher Scientific, #15140122), 1% GlutaMAX (Thermo Fisher Scientific, #35050038). Cells were grown in humidified incubator at 37°C, 5% CO₂ and 5% O₂. DLD-1 expressing mAID-mClover-POLR2A and Tet-OsTIR1 cells (Nagashima et al., 2019), were grown at 37°C in 5% CO₂ in RPMI-1640 (Sigma-Aldrich, #R8758) medium supplemented with 10% FBS.

METHOD DETAILS

Inhibition of transcription and topoisomerase

Inhibition of transcription experiments were performed as described (Busslinger et al., 2017). Briefly HeLa, IMR90 and U2OS cells were plated at high confluence (30.000 - 40.000 cells/cm²) and growth medium was replaced with resting medium (2% FBS, 1% Penicillin-Streptomycin in DMEM) for 24h before treatment. Inhibitory drugs were diluted in resting medium at the final concentrations listed in Table S4, treatments were performed from 0.5 to 7.5h. Unless specified, treatments were performed for 5h. For DRB washout experiment, medium containing DRB was removed, cells were washed with PBS and were incubated for 24h with fresh resting medium. For RNAP I inhibition, after incubation of the cells with resting medium for 24h, cells were treated with CX-5461 for 2h as described (Nagashima et al., 2019). For acute degradation of RPB1, cells were incubated in growth medium supplemented with 1 µg/ml doxycycline and with 500 µM indole-3-acetic acid for 24 h; solvent, concentration and product codes are listed in Key Resource Table and Table S4. For topoisomerase 1 and 2 inhibition, cells were treated with b-lapachone and Doxorubicin respectively, concentrations and codes are listed in Table S4. For both inhibitors, cells were growth in resting medium for 24h prior to addition of inhibitors, treatments were performed from 1 to 5h. For all inhibitors, specific time of treatments are specified at corresponding figures.

For OligoSTORM and experiments requiring simultaneous imaging of DNA and proteins in super-resolution, fluorescent amino-yellow beads were added (1:800 dilution, SpheroTech, #AFP-0252-2) during the last hour of treatment. Beads were later used for drift correction and further adjustments (see section STORM imaging).

For imaging purposes cells were plated in borosilicate glass bottom 8-well chambers (Nunc Lab-Tek, #155411 or µSlide Ibidi, #80827) and for gene or protein expression analyses the cells were plated in 6-well plates or 10 cm dishes. Immediately after treatment, cells were fixed in PFA 4 % (Alfa Aesar, #43368) diluted in PBS for imaging purposes or harvested by scraping for gene and protein expression analyses.

EdC incorporation and DNA labeling

To label DNA, a 48h incorporation of EdC (Sigma-Aldrich, #T511307) at 5 μ M concentration was performed in HeLa and DLD-1 cells. Cells were plated in chambered coverglass (Nunc Lab-Tek, #155411 or μ Slide Ibidi, #80827) at a concentration of 24.000 cells/cm² in growth medium supplemented with EdC for 24 h. The following day growth medium was replaced by resting medium supplemented with EdC and incubated for another 24 h. For DLD-1 cells Doxycycline was added together with EdC for the last 24 h. At the end of EdC incorporation, cells were treated with the different inhibitors as previously described (see section Inhibition of transcription and topoisomerase). Cells were fixed with PFA 4% (Alfa Aesar, #43368) for 10 min at room temperature and then rinsed with PBS three times for 5 min each. Cells were permeabilized with 0.3% Triton X-100 in PBS for 15 min and rinsed with PBS three times for 5 min each. Click chemistry reaction was performed by incubating cells for 30 min at room temperature in click chemistry buffer [150 mM Hepes pH 8.2, 50 mM Amino Guanidine (Sigma-Aldrich, #396494), 100 mM L-Ascorbic Acid (Sigma-Aldrich, #A92902), 1 mM CuSO₄ (Sigma-Aldrich, #C1297), 2% Glucose (Sigma-Aldrich, #G8270), 0.1 % Glox solution (described in STORM imaging) and 20 μ M AF647 azide (Thermo Fisher Scientific, #A10277)] protected from light. After three washes with PBS, we directly proceeded with STORM imaging for single color DNA imaging experiments (see section STORM imaging) or with immunolabeling for combined DNA and protein imaging experiments (see section Immunolabeling for confocal, STORM and DNA-PAINT).

EU incorporation and nascent RNA labeling

To label RNA, a 1h of EU incorporation at 1 mM concentration was performed in HeLa cells, using the Click-iT RNA Alexa Fluor 488 Imaging Kit (Thermo Fisher Scientific, #C10329). Cells were plated in chambered coverglass (μ Slide Ibidi, #80827) at a concentration of 30.000 cells/cm² in growth medium for 24 h. The following day growth medium was replaced by resting medium and incubated for

other 24 h. The third day, cells were cultured in resting medium and treated with ActD at multiple time points or with DMSO for 5h as mock control. During the last hour of treatment, medium was replaced with new treatment medium supplemented with EU working solution.

Cells were fixed with PFA 4% (Alfa Aesar, #43368) for 10 min at room temperature and then rinsed with PBS three times for 5 min each. Cells were permeabilized with 0.3% Triton X-100 in PBS for 15 min and rinsed with PBS three times for 5 min each. Click-iT reaction was performed following manufacturer's instructions by incubating cells with 1X Click-iT reaction cocktail freshly prepared with Alexa Fluor 488 azide for 30 min at room temperature, protected from light. Cells were washed once with Click-iT reaction rinse buffer and then with PBS. For DNA staining, cells were incubated with Hoechst 33342 at a 1:1000 dilution, for 15 min at room temperature. Cells were washed twice for 5 min each with PBS buffer and then imaged by confocal microscopy (see confocal imaging section).

Immunolabeling for confocal, STORM and DNA-PAINT

Cells were fixed with PFA 4% (Alfa Aesar, #43368) for 10 min at room temperature and then rinsed with PBS three times for 5 min each. Cells were permeabilized with 0.3% Triton X-100 in PBS and blocked in blocking buffer (10% BSA – 0.01 % Triton X-100 in PBS) for one hour at room temperature. Cells were incubated with primary antibodies (see Key Resource Table) in blocking buffer at 1:50 dilution for super-resolution imaging (STORM and DNA-PAINT) and at 1:100 dilution for confocal imaging. Cells were washed three times for 5 min each with wash buffer (2 % BSA – 0.01 % Triton X-100 in PBS) and incubated in secondary antibody (see Key Resource Table). For confocal imaging, commercial AlexaFluor conjugated secondary antibodies (Thermo Fisher Scientific, see Key Resource Table) were added at a 1:500 dilution in blocking buffer and were incubated for 45 min at room temperature. For STORM imaging, home-made (Bates et al., 2007) dye pair labeled secondary antibodies (see Key Resource Table) were added at a 1:50 dilution in blocking buffer and were incubated for 45 min at room temperature. For DNA-PAINT imaging, docking strand labeled secondary antibodies (Ultivue-2, or

Massive Photonics, see Key Resource Table) were added at a 1:100 dilution in Antibody dilution (Ultivue-2 plex or Massive Photonics) and were incubated for 1.5 h at room temperature. Cells were washed three times for 5 min each with wash buffer. For confocal imaging, DAPI was added for 10 min at room temperature before washes.

STORM imaging

Single molecule localization microscopy (SMLM) imaging was performed on a N-STORM 4.0 microscope (Nikon) equipped with a CFI HP Apochromat TIRF 100x 1.49 oil objective and an iXon Ultra 897 camera (Andor) and using Highly Inclined and Laminated Optical sheet illumination (HILO).

For single color STORM imaging of proteins (Figure S1E S4I and S5G), sequential imaging acquisition was performed (1 frame of 405 nm activation followed by 3 frames of 647 nm reporter) with 10 ms exposure time for 60000 frames. 647 nm laser was used at constant $\sim 2 \text{ kW/cm}^2$ power density and 405 nm laser power was gradually increased over the imaging.

For dual color STORM imaging of two different proteins (Figure S1G, 3G, S4B and F), double activator and single reporter strategy was used by combining AF405_AF647 anti-Mouse secondary with Cy3_AF647 anti-Rabbit secondary antibodies. Sequential imaging acquisition was performed (1 frame of 405 nm activation followed by 3 frames of 647 nm reporter and 1 frame of 560 nm activation followed by 3 frames of 647 nm reporter) with 10 ms exposure time for 120000 frames. 647 nm laser was used at constant $\sim 2 \text{ kW/cm}^2$ power density and 405 nm and 560 nm laser powers were gradually increased over the imaging.

For single color STORM imaging of DNA (Figure 2A, 4B, 5E, 6B and Figure S3A, C), continuous imaging acquisition was performed with simultaneous 405 and 647 nm illumination of the sample, 10 ms exposure time for 60000 frames. 647 nm laser was used at constant $\sim 2 \text{ kW/cm}^2$ power density and 405 nm laser power was gradually increased over the imaging.

To image DNA together with proteins in two-colors, combined STORM and DNA-PAINT approach was used. For combined STORM and DNA-PAINT imaging

(Figure 1A, D, E, 3A, C, 4B, E, 5A, 6E and Figure S3E) a Dual View system (Optosplit-II Cairn Research housing with a T647lpxr dichroic beamsplitter from Chroma) was used in combination with the imaging strategy described in Otterstrom et al (Otterstrom et al., 2019). The dual view allowed to split the image on the full chip of the camera based on emission wavelength. 647 nm laser was used to excite the DNA labeled with AlexaFluor 647 using a power density of ~ 2 kW/cm². Simultaneously, to perform DNA-PAINT, the 560 nm laser was used with ~ 1 kW/cm² power density to excite Atto-568 (Massive Photonics) or Cy3-equivalent dye (Ultivue) attached to the imager strands. The 488 nm laser at ~ 0.05 kW/cm² power density was used to illuminate the fiduciary beads, which were used for drift correction and chromatic alignment. Images were acquired at 20 ms per frame in continuous mode. The imaging cycle was composed by 100 frames of simultaneous, 560 nm and 647 nm activation interspersed with one frame of 488 nm illumination. The yellow beads imaged with the 488 nm laser were visible in both the red and orange channel, albeit dimly in the red channel.

The N-STORM cylindrical lens adaptor was used for STORM+DNA-PAINT data acquisition to obtain 3D localization data (Figure 1D, E), as previously described (Huang et al., 2008). Briefly, calibration data was first acquired by imaging sub-diffraction limit size beads (100 nm Tetraspeck, Thermo Fisher Scientific, #T7279) in PBS adsorbed borosilicate chamberslides. Using the NIS software STORM module, Z-calibration data was recorded as the microscope stage was moved in 10 nm steps over a 1.6 μ m range and through the objective focal plane to image the elliptically shaped beads as they first elongated vertically, then horizontally.

Imaging buffer composition for STORM imaging was [100 mM Cysteamine MEA (Sigma-Aldrich, #30070) - 5% Glucose (Sigma-Aldrich, #G8270) – 1% Glox Solution (0.5 mg/ml glucose oxidase, 40 mg/ml catalase (Sigma-Aldrich, #G2133 and #C100)] in PBS.

Imaging buffer composition for combined STORM and DNA-PAINT imaging was 100 mM Cysteamine MEA, 5% Glucose, 1% Glox Solution, 0.75 nM Imager strand (I1-560 and I2-560 for mouse and rabbit secondary antibodies respectively, Ultivue) in Ultivue Imaging Buffer or 100 mM Cysteamine MEA, 5% Glucose, 0.1% Glox

Solution, 1 nM Imager strand (Atto-568-ImagerStrand for rabbit secondary, Massive Photonics) in PBS 500 mM NaCl.

Super-resolution images were analyzed and rendered in Insight3 (kind gift of Bo Huang, UCSF) as described (Bates et al., 2007; Rust et al., 2006). Specifically, Point Spread Functions (PSFs) from the emission from single fluorophores were identified at individual frames of the acquired videos, based on a set threshold of intensity. They were fit to a two-dimensional Gaussian. From it, the centroid of the PSF was obtained, and from it the x and y positions for 2D STORM imaging were obtained. For 3D STORM images (Figure 1D, E), 3D localizations were obtained using the procedure already described by fitting the PSFs obtained during imaging with a 2D elliptical Gaussian function, from which we obtained the x and y positions as well as the peak widths w_x and w_y , which in turn allowed the z coordinate of the fluorophore to be determined based on our calibrations. As the precision is reduced from the distance to the focal plane, 200 nm thick z-slices centered in $z=0$ were selected. Sample drift during acquisition was calculated and subtracted by cross-correlation drift correction. The cross-correlation function between subsets of frames (typically 1000 frames per subset) were obtained and the transformation function was calculated. From this, the localizations positions were corrected based on its frame of acquisition. 2D images were rendered by representing each localization (i.e. x-y positions) as a two-dimensional Gaussians with fixed width. For 3D images, localizations were rendered using a three-dimensional, fixed size Gaussian. DNA data was uniformly colored in white. RNA Pol II phSer2 localizations were colored based on their z-position relative to the focus point ($z=0$). For combined STORM and DNA-PAINT imaging both 2D and 3D, we followed the analysis workflow described in Otterstrom et al (Otterstrom et al., 2019).

Specifically, the localization lists for the STORM signal (DNA) and the bead emission in the < 647 nm half of the image were obtained in Insight3 from the original movie. To obtain DNA-PAINT and 647-nm-emission bead signals, we first performed a frame summation for every five frames of DNA-PAINT imaging, and another frame summation for every five frames of beads. From the DNA-PAINT summated movie, we obtained the DNA-PAINT list in Insight3. From the summation

of the beads we obtained the bead list in the 647 nm half of the image in Insight3. The trajectory of the beads was used to calculate the drift over time and correct the localizations independently for each channel. The drift-corrected beads were then paired between the two spectral halves of the image to obtain a 2D affine transformation to overlap the spectrally separated signals. For 3D STORM DNA-PAINT, we also performed a final axial (z) alignment using the fiduciary beads z-position.

Confocal imaging and quantification

Confocal images were taken on a Leica TCS SP8 confocal microscopy equipped with HC Plan-Apochromat CS2 63x/1.40 oil lens, using LAS X Software (Leica). Full nuclear volumes or single stacks were acquired at 400 Hz, Pinhole 1, and optimized z stack steps of 300 nm. Fluorescence intensity quantification has been performed in ImageJ (2.0.0) by generating masks for each nucleus using Hoechst/DAPI signal as reference and registering the mean intensity of the proteins of interest (Figure S6C) or of EU-AF488 signal (Figure S2G). For Pearson correlation analysis (Figure S1F) and 3D volume renderings (Movie 1), images of 100 nm Tetraspeck beads (Thermo Fisher Scientific, #T7279) were acquired for every channel to be used as reference for chromatic aberration correction performed with Huygens 17.10.0p5 software (see section Pearson correlation and 3D Rendering).

Oligopaint probe design and probe synthesis

Oligopaint probes were designed *in silico* by using Oligominer balanced setting (blockParse.py with balanced flag '-l 35 -L 41 -t 42 -T 47') (Beliveau et al., 2018) to a repeat-masked hg19 human genome assembly against the following coordinates Chr12: 6,641,500-6,666,000 (24.5 kb) and Chr6: 31,095,000-31,173,000 (78 kb), corresponding to *GAPDH-IFFO1* and *OCT4-TCF19* loci, respectively. 286 probes targeting *GAPDH-IFFO1* and 384 probes against *OCT4-TCF19* were generated. Oligominer scripts are available through Github (<https://github.com/brianbeliveau/OligoMiner>).

Oligopaint libraries were synthesized as 12K oligopools (CustomArray - Genscript) and after a quality check assessment by qPCR (see Table S5), they were amplified as previously described (Beliveau et al., 2017). Briefly, probes for *GAPDH-IFFO1* and *OCT4-TCF19* loci were amplified from the library by PCR (Kapa Taq PCR kit, Kapa Biosystems, #BK1002) and T7 promoter sequences were added to the amplicons by touch up PCR (see Table S5). Amplicons were then subjected to T7 RNA polymerase mediated *in vitro* transcription (HiScribe T7 High Yield RNA Synthesis Kit, NEB, #E2040S) followed by a reverse transcription reaction (Maxima H Minus RT, Thermo Fisher Scientific, #EP0752) using 5' AF405 labeled primers (see Key Resource Table and Table S5). Reverse transcription reaction products were mixed with 0.5 M NaOH and 0.25 M EDTA solution (1:1 v/v) and incubated at 95° C for 10 min to degrade RNA by alkaline hydrolysis. Probes were finally purified and concentrated with DNA Clean & Concentrator–100 kit (Zymo Research, #D4030) to obtain ssDNA probes.

Sample preparation and OligoSTORM labeling

IMR90 fibroblasts were plated and treated with ActD or DMSO as previously described (see section Inhibition of transcription). After fixation with 4% PFA, cells were prepared for OligoSTORM as previously described (Beliveau et al., 2017). Briefly, cells were permeabilized with 0.5% Triton X-100 in PBS for 10 min and with 0.1 % Tween in PBS for 2 min at room temperature. Cells were then incubated for 5 min in 0.1 N HCl and washed twice with 2xSSCT for 1 min each, followed by a 5 min wash at room temperature in 2x SSCT - 50% Formamide (Sigma-Aldrich, #F9037) and stored for up to one week in 2x SSCT - 50% Formamide at 4° C or used immediately for imaging. Before hybridization, the samples were incubated in 2x SSCT - 50% Formamide at 60° C for 20 min. Then, the hybridization mix is prepared (2x SSCT, 50% Formamide, 10% (w/v) dextran sulfate (Sigma-Aldrich, #S4030), 0.4 µg/µL of RNase A (Thermo Fisher Scientific, #EN0531), 50 pmoles of 5' AF405 labeled primary probes and 1µl 100 µM 3' AF647 labeled secondary probes) (see Key Resource Table and Table S5), added to the samples, denatured at 78° C for 3 min and subsequently incubated at 42° C for 16 h. Samples were

washed twice with 2x SSCT at 60°C for 10 min each, once with 2x SSCT for 10 min at room temperature and once with 2x SSC.

OligoSTORM imaging

OligoSTORM samples were imaged on a N-STORM 4.0 microscope (Nikon) equipped with a CFI HP Apochromat TIRF 100x 1.49 oil objective and an iXon Ultra 897 camera (Andor) and HILO illumination mode. Conventional fluorescence images were taken at the beginning of each imaging cycle to register the position of loci and fiduciary beads. STORM images were acquired using continuous imaging acquisition mode with simultaneous 405 and 647 nm illumination of the sample with 16 ms exposure time for 60000 frames. 647 nm laser was used at constant $\sim 2 \text{ kW/cm}^2$ power density and 405 nm laser power was gradually increased over the imaging. Every 100 frames, one frame of 488 nm illumination was taken to image fiduciary beads used for drift correction.

The imaging buffer composition for STORM imaging was 100 mM Cysteamine MEA (Sigma-Aldrich, #30070) – 1% Glox Solution (0.5 mg/ml glucose oxidase, 40 mg/ml catalase (Sigma-Aldrich, #G2133 and #C100) - 5% Glucose (Sigma-Aldrich, #G8270) in PBS. A diffraction limited image was taken at the beginning of each imaging session.

OligoSTORM images were analyzed and rendered in Insight3 as previously described (Bates et al., 2007; Rust et al., 2006). Localizations were identified based on a threshold and fit to a simple Gaussian to determine the x and y positions. Conventional and STORM images were overlapped to verify the position of *GAPDH-IFFO1* and *OCT4-TCF19* loci. Loci areas were manually selected in ImageJ and were used for Voronoi tessellation and Radius of gyration analysis (see sections Voronoi tessellation and Radius of gyration).

Voronoi tessellation and cluster analyses

Voronoi Tessellation Analysis was performed in Matlab as previously described (Andronov et al., 2016). A Voronoi diagram was computed using the list of STORM localizations (voronoin.m). Then the areas of the Voronoi polygons were

determined from the Voronoi vertices and the Voronoi cells of the Voronoi diagram (polyarea.m). The local density in each data point was defined as the inverse value of the area of the corresponding Voronoi polygon. Cumulative distribution functions of the density values were plotted.

To assess the size and morphology of SMC1A clusters as individual clusters and as vermicelli structures (Figure 5C, D, and S5G) Voronoi tessellation was followed by cluster identification. After Voronoi tessellation, a threshold based on polygon area is established. Localizations having polygon areas below the threshold belong to clusters. This threshold is obtained by intersecting the experimental Voronoi area distribution with that of an averaged distribution obtained from Monte Carlo simulations of randomized localizations drawn from an area corresponding to the original data. A minimum number of 5 localizations per cluster was used. The area of clusters was obtained by summation of the polygon areas of the localizations that comprise a cluster.

To analyze cohesin clusters in terms of size of individual clusters (Figure 1B, C and S3H, I), cluster analysis was performed as previously described (Ricci et al., 2015). Specifically, the localization lists were binned to construct discrete localization images with a pixel size of 10 nm and pixel intensity equal to the number of localizations falling in the corresponding pixel. These images were convoluted with a 5x5 pixels kernel to obtain density maps and transformed into binary images by applying a constant threshold, such that each pixel has a value of either 1 if the density surpasses the threshold value and 0 if not. Localizations falling inside a 0-value area of the image were discarded. Cluster centroids were obtained from local maxima of the density map, and localizations were assigned to clusters using a distance-based algorithm. New cluster centroids were then calculated as the average of the localizations previously assigned to the cluster. This process was repeated iteratively until convergence of the sum of the squared distances of the localizations belonging to the cluster and the centroid. Final centroid position and number of localizations were obtained for each cluster. Cluster sizes were calculated as the standard deviation of x-y coordinates from the centroid of the cluster.

Quantification of DNA-free areas

DNA-free area was quantified from DNA STORM images by applying a binary threshold on a Gaussian filtered density map (imbinarize.m Matlab function, with adaptive threshold, sensitivity of 0.001, pixel size 20 nm, sigma 2). Percentage of DNA-free areas over the imaged nuclear area were estimated for each nucleus.

Coefficient of variation analysis

For the assessment of chromatin compaction through the Coefficient of Variation (CV) analysis, DAPI stained cells (see section Immunolabeling for confocal, STORM and DNA-PAINT) treated with the different inhibitory drugs were imaged on a Leica TCS SP8 confocal microscope (see section Confocal imaging). Central sections of the nuclei were used to measure the CV. We generated a work-flow in ImageJ 2.0.0 consisting of the creation of masks corresponding to the nuclei which were then applied to the raw image to allow the selection of single nuclei. The coefficient of variation (CV) of individual nuclei was calculated in Matlab, with $CV = \sigma / \mu$, where σ represents the standard deviation of the intensity values and μ representing the mean value of intensity of the nucleus.

Radius of gyration analysis

Radius of gyration (Rg) of loci obtained by OligoSTORM was calculated with Matlab as the root-mean square distance of localization positions in each domain from the centroid of these positions in the domain (Boettiger et al., 2016).

Colocalization index analysis – STORM imaging

Pixel colocalization was quantified by calculating the percentage of overlaying pixels between binary masks of the protein of interest (EZH2, H3K9 or SMC1A) with the binary mask of DNA. First, binary masks were derived from the density maps of DNA and proteins using imbinarize.m Matlab function (with adaptive threshold and sensitivity of 0.1). Then, the colocalization was calculated as number of overlapping pixels. In order to correct for the different values of DNA area, we

have weighted the percentage of overlying pixels considering the distribution of DNA areas for the different cells.

$$Colocalization_{weighted} = \frac{Colocalization}{Cell_DNA_Area} \cdot Max_DNA_Area$$

Gene expression analysis

RNA extraction was performed with RNeasy Mini Kit (QIAGEN) and reverse transcription was carried out with iScript cDNA Synthesis Kit (BIO-RAD, #1708891). qPCR was performed with Lightcycler 480 SYBR green I master (Roche, #4887352001) and the primers listed in Table S6 and plates were run on a Lightcycler 480 (Roche) qPCR instrument.

For RNA-seq, we used ribosomal depletion to remove rRNAs from total RNA samples, then proceed with library construction using Illumina TruSeq chemistry. Libraries are then sequenced using Illumina NovaSeq 6000 at Columbia Genome Center. We multiplexed samples in each lane, which yields targeted number of paired-end 100bp reads for each sample. We used RTA (Illumina) for base calling and bcl2fastq2 (ver. 2.20) for converting BCL to fastq format, coupled with adaptor trimming. Reads were pseudoaligned to a Kallisto index created from GRCh38 Ensembl v92 transcriptome using Kallisto (ver. 0.44.0) (Bray et al., 2016).

Protein extraction, WB and protein quantification

Cells were harvested by scraping with a cell lifter and collected into microcentrifuge tubes. Samples were processed as previously described (Beringer et al., 2016). Specifically, cell pellets were washed with cold PBS and resuspended in 2.5x packed cell volume of PBS and an equal volume of 2x SDS lysis buffer (50 mM Tris HCl pH 7.5, 2 mM EDTA, 2 % SDS). Samples were boiled for 10 min and sonicated for 5 min (High power, 30 sec ON – 30 sec OFF cycles). Protein extracts were quantified with Pierce BCA Protein Assay Kit. Protein extracts (1 to 10 ug) were loaded on 4–15% precast protein gels (Mini-PROTEAN TGX, Bio-Rad, #4561084). Membranes were incubated with rabbit cell cycle WB cocktail (Cdk pTyr15, H3 pSer10, actin) (Abcam, #ab136810), rabbit anti-SMC1A (Abcam, #ab133643),

rabbit anti-SMC3 (Abcam, #ab128919), and mouse anti-vinculin 1:1000 (Sigma, #V9131) and with secondary antibodies sheep anti-Mouse IgG HRP-linked 1:1000 (GE Healthcare, #NA931), Donkey anti-Rabbit IgG HRP-linked 1:2000 (GE Healthcare, #NA934). HRP-derived signal was detected with Pierce ECL Western Blotting Substrate kit (Thermo Fisher Scientific, #32106) on an Amersham Imager 600 (GE Healthcare Life Sciences, # 29083461). Quantification of western blots was performed by Image Studio Lite 5.2 software (LI-COR), protein levels were normalized to Vinculin.

Single molecule tracking imaging and analysis

SMT experiments for RAD21 cohesin subunit were performed in SNAP-H3.3 + RAD21-Halo U2OS cells previously described by (Rhodes et al., 2017b) and kindly provided by Dr. Kim Nasmyth (University of Oxford). After ActD or DMSO treatments (see section Inhibition of transcription), cells were labeled with 1 nM JF549-SNAP ligand and 4 pM (for studying the dissociation kinetics) or 10 pM (for studying the fast dynamics) JF646-Halo ligand diluted in phenol red free resting medium for 30 min in the incubator. Cells were washed once for 15 min in the incubator with fresh medium and then once for 5 min. Cells were imaged immediately after staining or fixed after labeling and subsequently imaged. JF549 SNAP ligand and JF646 Halo ligand were a kind gift from Dr Luke Lavis (Janelia Research Campus) (Grimm et al., 2015).

Imaging was performed using a N-STORM 4.0 microscope (Nikon) equipped with an Okolab cage incubator system set at 37C, 5% CO₂ and controlled humidity. Images were taken with a 100X 1.49 oil objective, an iXon Ultra 897 camera (Andor), using HILO illumination and a quad-band emission filter. RAD21-Halo^{JF646} cells labeled with 4 pM JF646-Halo ligand were imaged for 600 frames with 500 ms of exposure time at 1% power of 647 nm laser. RAD21-Halo^{JF646} cells labeled with 10 pM JF646-Halo ligand were imaged for 10000 frames with 15 ms exposure time at 8% power of 647 nm laser. In both cases, the area occupied by nuclei was determined by imaging four frames of JF549-SNAP-H3.3 at the beginning and at the end of each SMT video. Fixed samples were acquired under the same

experimental conditions and used as reference for photobleaching correction (see details below).

For the data analysis, first, the images were segmented by manually selecting the nuclear areas from SNAP-H3.3 signal, corresponding to each cell nucleus. The localization of the single molecules and the connection of the trajectories was done using TrackMate, an open source ImageJ plugin (Tinevez et al., 2017). For the detection, the LoG detector with sub-pixel localization was used and the Simple LAP tracker was used for the tracking, with a maximum frame gap of 4 and 2 frames for 500 and 15 ms data respectively. The intensity threshold for the localizations was defined to minimize false localizations: 70 for the 500 ms data, and 30 for the 15 ms data. The trajectories were analyzed using a custom written Matlab code, that makes use of some functions from @msdanalyzer (Tarantino et al., 2014). For the analysis of the trajectories from 15 ms exposure time. The trajectories were classified into different motion types: confined, Brownian and directed. This was done by fitting a power law function to each individual T-MSD curve:

$$MSD = 4 \cdot D \cdot t_{lag}^{\alpha}$$

Where D is the diffusion coefficient and t_{lag} is the time lag between the different time points of the track. Trajectories with $\alpha < 0,8$ were considered as confined, with $0,8 < \alpha < 1,2$ as Brownian, and with $\alpha > 1,2$ as directed. In addition, the trajectories performing confined motion and free diffusion together were identified, separated and segmented in multiple parts.

The radius of confinement of the whole population of trajectories was estimated by fitting a confined circle diffusion model to the ensemble of confined trajectories with average frame-to-frame jumps below 150 nm (Wieser and Schutz, 2008):

$$MSD = R^2 \cdot \left(1 - e^{\frac{-4Dt_{lag}}{R^2}} \right) + 0$$

Where R is the radius of confinement and D , the diffusion coefficient at short term mobility. O is an offset value that comes from the localization precision limit of SMLM techniques. In this case, we have estimated a localization precision of around 35 nm from the fitting of the experimental data.

For the 500 ms data, all the trajectories were analyzed, considering that a one-frame localization is a binding event which has a residence time of 500 ms. The dissociation kinetics were estimated from the track length of each individual trajectory, by fitting a two-component exponential decay function to the survival function defined by: (1 – Cumulative Distribution Function) (Ball et al., 2016; Chen et al., 2014; Mazza et al., 2012):

$$F(t) = f \cdot e^{-k_1 \cdot t} + (1 - f) \cdot e^{-k_2 \cdot t}$$

Where f is the fraction belonging to each population, k_1 the short-live component associated with unspecific chromatin binding and k_2 the long-live component associated with specific chromatin binding.

This residence time measurements are affected by photobleaching. In order to correct for it, we fixed the cells and then imaged and tracked them under the same experimental conditions (Hansen et al., 2017). Then we fitted an exponential decay function to their survival fraction:

$$F_b(t) = e^{-k_b \cdot t}$$

Where k_b is a constant that estimates the photo-bleaching rate in s^{-1} for a certain fluorophore and imaging conditions. The corrected dissociation rates are obtained from:

$$k_{measured} = k_{corrected} + k_{bleaching}$$

Where $k_{measured}$ corresponds to k_2 and $k_{bleaching}$ to k_b , from previous equations. Finally, the bleaching corrected residence times were obtained by:

$$Residence_Time = \frac{1}{k_{corrected}}$$

Note that the dissociation rates for fixed cells were smaller than those of live cells, assuring that measured residence times are related with protein unbinding due to live cell activity.

Nearest neighbor distance (NND) analysis

Cluster analysis of individual channels was performed as described in detail in section “Voronoi tessellation and cluster analyses” with the clustering method previously published (Ricci et al., 2015). NND between clusters’ centroids was calculated by `knnsearch.m` Matlab function and the NND histogram of experimental data was obtained by considering all the NNDs of individual nuclei (histogram bin, from 0 to 500 nm, 5 nm steps). Simulated NNDs recapitulating random spatial distribution of cluster centroids were first obtained for each nucleus separately and then merged to calculate the simulated NND histogram (histogram bin, from 0 to 500 nm, 5 nm steps). The difference plot reports the difference between experimental NND and simulated NND.

Cross pair correlation analysis

STORM data consist of two-dimensional spatially distributed centroids of the molecule’s diffraction limited spot, conforming a map of point locations. Hence, exploratory analysis of spatial point patterns (Baddeley et al., 2016; Shivanandan et al., 2016) is performed to seek evidences for possible stochastic dependence between SMC1A and H3K4me2, and SMC1A and SMC3, by computation of cross pair correlation functions of a so-called bivariate point pattern. Two to three regions of interest of size $2 - 10 \mu\text{m}^2$ were selected for every nucleus, and the empirical cross pair correlation $G(r)$ was computed from $r = 0$ to 200 nm interpoint distances at 3.2 nm step size. If $G(r) > 1$, it exists a stochastic dependency between points at distance r , which can be consistent with clustering behavior. At distances where $G(r) = 1$, the points are not correlated. Note that at $r=0$ there is a missing value, as the cross pair correlation is infinity at the origin.

All simulations were done in R (RCoreTeam, 2014), using the `spatstat` module (Baddeley et al., 2016) and custom functions.

Generation of SMC1A and SMC3 knockdown cells

HeLa *SMC1A*, *SMC3* knockdowns and non-silencing (NS) controls were generated by transduction of pLKO.1_puro lentiviral vectors containing shRNA for *SMC1A*, *SMC3* and control (Sigma-Aldrich, *SMC1A* NM_006306, TRCN0000299517; *SMC3* NM_005445, TRCN0000234318; NS #SHC002). Lentiviral production has been performed following The RNAi Consortium (TRC) low throughput viral production protocol (<https://portals.broadinstitute.org/gpp/public/resources/protocols>). Transduced cells were selected for puromycin resistance (Sigma-Aldrich, #540141). Efficiency of knockdowns was verified at the level of RNA (Figure S6B) by qPCR (see section Gene Expression Analysis) and at the level of protein abundance (Figure S6A, C) by WB (section Protein extraction, WB and protein quantification) and immunofluorescence.

Generation of WAPLΔ cells

Cells were transfected with pX458 plasmid encoding for Cas9, GFP and a sgRNA targeting M1116 codon of *WAPL* gene (5'- GCATGCCGGCAAACACATGG -3') (Rhodes et al., 2017a) or without sgRNA as negative controls. pSpCas9(BB)-2A-GFP (pX458) was a gift from Feng Zhang (Addgene plasmid #48138). Transfections were performed in a 3:1 ratio with Fugene HD (Promega, #E2311) and GFP positive cells were isolated by cell sorting (Influx and FACS Aria) 48 h post transfection. For generation of clonal populations, GFP⁺/DAPI⁻ cells were sorted as single cells and collected in 96 well plates while for the remaining cases, cells were sorted as bulk GFP⁺/DAPI⁻ populations. Sorted cells were subsequently expanded and screened by sequencing to identify the type of mutations generated on *WAPL* gene (Figure S1D). Since HeLa cells are triploid, selected clones displayed mutations on the three alleles.

When specified, grown in EdC-supplemented medium and treated with specific inhibitors (see sections EdC labeling and inhibition of transcription, acute RNAP II degradation and inhibition of topoisomerases). To assess the percentage of cells

with vermicelli (Figure 5B, G, 6G and S5A-F, S7E), cells were labeled against SMC1A or SMC3 and DAPI (see section Immunolabeling) and imaged by confocal microscopy (see section Confocal imaging and quantification). Vermicelli morphology was determined as previously described (Tedeschi et al., 2013). Specifically, the percentage of nuclei with vermicelli morphology (i.e. elongated worm-like signal of SMC1A/SMC3) over the total number of nuclei was quantified manually by visual analysis of SMC1A/SMC3 and DAPI staining, in ImageJ.

Lamin A/C and H3K9me3 quantification at nuclear edge

The percentage of Lamin A/C and H3K9me3 localizations at the edge of nucleus was calculated using a custom Matlab script, according to the following procedure. First a Gaussian filtered density map of Lamin A/C and H3K9me3 STORM coordinates was generated (pixel size 20 nm, sigma 3), then an edge of 400 nm was drawn around the nuclear rim. The percentage of localization falling in this edge was calculated as the number of localizations inside the edge region divided by the total number of localizations inside the nucleus.

Pearson correlation analysis

In order to analyze the colocalization between DNA and RNAP II phSer2 and between DNA and SMC1A we performed confocal imaging of entire nuclear volumes of WAPLΔ cells with vermicelli morphology stained for SMC1A, RNAP II phSer2 and DAPI (see sections Immunolabeling and Confocal imaging and quantification). To avoid biases derived from chromatic aberration we first performed chromatic aberration correction (CAC) with the CAC module of Huygens software. To establish the correction parameters, we used as reference Tetraspeck beads imaged in the same experimental conditions than our biological samples. After CAC, we deconvolved the images with the Deconvolution express module of Huygens with conservative deconvolution profile. Next, we proceeded with colocalization analysis by estimating the Pearson correlation coefficient for DNA vs RNAP II phSer2 and DNA vs SMC1A within the nuclei volumes using the Huygens colocalization wizard with optimized thresholding mode.

ChIP-seq experiments and analysis

Chromatin immunoprecipitation (ChIP) for HeLa cells was performed as described (Neguembor et al., 2013) with the following modifications. For each IP, 50 ug of chromatin were incubated with 30 ug of H3K4me2 (Millipore, #07-030) antibody. IPs were washed twice with wash buffer 1 (20 mM Tris-HCl pH 8, 2 mM EDTA pH 8, 1 % Triton-X100, 150 mM NaCl, 0.1 % SDS), twice with wash buffer 2 (20 mM Tris-HCl pH 8, 2 mM EDTA pH 8, 1 % Triton-X100, 500 mM NaCl, 0.1 % SDS), twice with wash buffer 3 (10 mM Tris-HCl pH 8, 1 mM EDTA pH 8, 0.5 % NP-40, 0.5 % Deoxycholate), and twice with TE (10 mM Tris-HCl pH 8, 1 mM EDTA pH 8). Chromatin was eluted twice by incubating beads in elution buffer (25 mM Tris-HCl pH 8, 5 mM EDTA pH 8, 0.5 % SDS) for 20 min at 65C in agitation. Samples were then incubated with RNase A (Sigma-Aldrich, #R5503) and Proteinase K (Sigma-Aldrich, #P2308) for 1 h at 37C and crosslinking was reverted by incubating samples overnight at 65C. DNA was purified by phenol-chloroform extraction and ethanol precipitation. DNA was resuspended in 10 mM Tris-HCl pH 8 and processed for sequencing. Libraries were prepared using the NEBNext Ultra DNA Library Prep for Illumina kit (#E7370) according to the manufacturer's protocol. Briefly, input and ChIP enriched DNA were subjected to end repair and addition of "A" bases to 3' ends, ligation of adapters and USER excision. All purification steps were performed using AgenCourt AMPure XP beads (Beckman Coulter, #A63882). Library amplification was performed by PCR using NEBNext Multiplex Oligos for Illumina. Final libraries were analyzed using Agilent Bioanalyzer or Fragment analyzer High Sensitivity assay (#5067-4626 or #DNF-474) to estimate the quantity and check size distribution, and were then quantified by qPCR using the KAPA Library Quantification Kit (KapaBiosystems, #KK4835) prior to amplification with Illumina's cBot. Libraries were sequenced 1 x 50 bp on Illumina's HiSeq2500.

Reads were filtered for low quality ones using fastp (Chen et al., 2018) and were aligned to the GRCh38 human genome using STAR ver. 2.5.21 in end-to-end mode and using '--alignIntronMax 1' to prohibit splicing and '--outFilterMultimapNmax 1' to keep only uniquely mapping read (Dobin et al., 2012). After removing duplicated

reads and pooling the replicates, peaks were called against the Input control sample using MACS ver. 3.0.0a5 with default parameters (Zhang et al., 2008).

H3K4me2 ChIP-seq peaks were annotated and classified using the ChIPseeker tool (Yu et al., 2015). Coordinates of active TSS were obtained from our RNA-seq dataset considering genes having an average detected expression > 2 Transcript Per Million (TPM) mapped reads. Number of active TSS with ≥ 1 H3K4me2 peak was obtained by overlapping active TSS with H3K4me2 ChIP-seq peaks.

Loop domains and expressed genes overlap estimation

Genomic coordinates for loop domains were obtained from Hi-C datasets (Rao et al., 2014) for GM12878, HeLa, K562, IMR90, HUVEC and NHEK cells, and from Micro-C (Krietenstein et al., 2020) for H1 cells. Gene coordinates and expression datasets for each of the abovementioned cell lines were obtained from ENCODE (GRCh37, Gencode v19 genes, see Key Resource Table).

First, the complete list of genes from Gencode v19 was intersected with loop coordinates (Krietenstein et al., 2020; Rao et al., 2014) from each corresponding cell line from. Genes were considered inside a loop if at least 50% of their annotated length was inside its genomic coordinates, otherwise genes were considered outside. Next, for each cell line, we calculated the transcript per million (TPM) values at each percentile of expression level (excluding genes with 0 TPM) by taking the mean TPM between the 2 replicates, and we counted the number of genes inside or outside loops (as previously defined) that were above the TPM threshold (expressed) or below (not expressed).

Fisher's exact test (Table S2) was performed to calculate the significance of preferential enrichment of expressed gene within loop domains.

The percentage of loops containing expressed genes at different expression levels (Table S3) was calculated by dividing the number of loops containing genes above the minimum threshold and over the 25, 50 and 75 percentiles of expression by the total number of loops in the corresponding cell type.

3D rendering - confocal imaging

Nuclei of WAPLΔ HeLa cells described in the previous section (Pearson correlation analysis) were rendered in 3D with Imaris 8.3.0 software (Oxford Instruments). After confocal imaging, CAC and deconvolution, the nuclear area was rendered in 3D. SMC1A signal (magenta) was rendered as a solid volume to highlight vermicelli structures, RNAP II phSer2 (green) was shown as sphere objects indicating the areas of accumulation of RNAP II phSer2 signal, DNA was represented in blue with partial transparency. Videos were created in Imaris with the animation module.

bTMP incorporation, imaging and quantification

bTMP incorporation and staining have been done as previously described (Naughton et al., 2013). Briefly, HeLa cells were plated in borosilicate chamberslides (μSlide Ibidi, #80827) and treatments with inhibitors were performed as described in the corresponding section (Inhibition of transcription, acute RNAP II degradation and inhibition of topoisomerases). At the end of treatments, cells were rinsed with 3xPBS and incubated with bTMP (1 mg/ml in PBS) for 20 min at room temperature in the dark followed by 10 min of UV crosslinking at 360 nm (UV 1800 Stratalinker, Stratagene). Stock solution of bTMP (kind gift of Dr Nick Gilbert) was prepared freshly (30 mg/ml in methanol) and further diluted in PBS to the final concentration just before use. As Mock controls DMSO-treated cells were incubated with methanol diluted in PBS. After three washes with PBS, cells were fixed with 4% PFA and washed again three times with PBS. Cells were permeabilized with 0.2% Triton X-100 in PBS for 10 min, blocked for 15 min with 5% Horse Serum (Gibco, #26050088) in PBS and incubated overnight at 4C with Streptavidin-AF488 (Thermo Fisher Scientific, #S11223) or NeutrAvidin-OG488 (Thermo Fisher Scientific, #A6374). DAPI was added for 10 min followed by three washes in PBS. Cells were imaged on N-STORM 4.0 microscope (Nikon) equipped with a CFI HP Apochromat TIRF 100x 1.49 oil objective and an iXon Ultra 897 camera (Andor) in epifluorescence illumination mode. The fluorescence signal derived from AF488-Streptavidin labelled bTMP was measure with ImageJ. We first used the DAPI signal to generate masks corresponding to the nuclear areas. We then applied the masks to the green channels to measure the mean intensity bTMP

value for each nucleus. We plotted the average intensity values for controls and WAPLΔ cells treated with bTMP as well as mock treated samples to establish levels of background signal.

QUANTIFICATION AND STATISTICAL ANALYSIS

Quantification and analysis have been performed in ImageJ (2.0.0), Matlab, R and Huygens (17.10.0p5) as previously specified for each case.

Statistical analysis has been performed in Graphpad Prism. For every dataset, normality tests (D'Agostino-Pearson and Shapiro-Wilk) were run to assess normal distribution. For datasets with Gaussian distribution of values, parametric tests were applied. In all cases two-tailed test were run and multiple comparison corrections were applied for datasets with more than two groups and multiple comparisons. For datasets with no Gaussian distribution, non-parametric tests were applied. The type of statistical test is specified in each case. Statistical significance is represented in the following manner: ns $p > 0.05$, * $p \leq 0.05$, ** $p \leq 0.01$, *** $p \leq 0.001$, **** $p \leq 0.0001$.

SUPPLEMENTAL VIDEO LEGENDS

Movie 1. RNA polymerase II preferentially localizes at the periphery of vermicelli structures, Related to Figure 1.

3D rendering of confocal images of WAPL Δ cells immunolabeled for SMC1A (magenta), RNAP II phSer2 (green) and DAPI-stained DNA (blue). Vermicelli structures are represented as volumes (magenta) and RNAP II phSer2 (green) points of local maximum intensity are rendered as spherical objects (green), confocal signal from DNA was shown with partial transparency (blue).

REFERENCES

- Andronov, L., Orlov, I., Lutz, Y., Vonesch, J.L., and Klaholz, B.P. (2016). ClusterViSu, a method for clustering of protein complexes by Voronoi tessellation in super-resolution microscopy. *Sci Rep* 6, 24084.
- Arner, E., Daub, C.O., Vitting-Seerup, K., Andersson, R., Lilje, B., Drablos, F., Lennartsson, A., Ronnerblad, M., Hrydziusko, O., Vitezic, M., *et al.* (2015). Transcribed enhancers lead waves of coordinated transcription in transitioning mammalian cells. *Science* 347, 1010-1014.
- Baddeley, A., Rubak, E., and Turner, R. (2016). Spatial point patterns : methodology and applications with R (Boca Raton ; London ; New York: CRC Press, Taylor & Francis Group).
- Ball, D.A., Mehta, G.D., Salomon-Kent, R., Mazza, D., Morisaki, T., Mueller, F., McNally, J.G., and Karpova, T.S. (2016). Single molecule tracking of Ace1p in *Saccharomyces cerevisiae* defines a characteristic residence time for non-specific interactions of transcription factors with chromatin. *Nucleic Acids Res* 44, e160.
- Baranello, L., Wojtowicz, D., Cui, K., Devaiah, B.N., Chung, H.J., Chan-Salis, K.Y., Guha, R., Wilson, K., Zhang, X., Zhang, H., *et al.* (2016). RNA Polymerase II Regulates Topoisomerase 1 Activity to Favor Efficient Transcription. *Cell* 165, 357-371.
- Barutcu, A.R., Blencowe, B.J., and Rinn, J.L. (2019). Differential contribution of steady-state RNA and active transcription in chromatin organization. *EMBO Rep* 20, e48068.
- Bates, M., Huang, B., Dempsey, G.T., and Zhuang, X. (2007). Multicolor super-resolution imaging with photo-switchable fluorescent probes. *Science* 317, 1749-1753.
- Beliveau, B.J., Boettiger, A.N., Avendano, M.S., Jungmann, R., McCole, R.B., Joyce, E.F., Kim-Kiselak, C., Bantignies, F., Fonseka, C.Y., Erceg, J., *et al.* (2015). Single-molecule super-resolution imaging of chromosomes and in situ haplotype visualization using Oligopaint FISH probes. *Nat Commun* 6, 7147.
- Beliveau, B.J., Boettiger, A.N., Nir, G., Bintu, B., Yin, P., Zhuang, X., and Wu, C.T. (2017). In Situ Super-Resolution Imaging of Genomic DNA with OligoSTORM and OligoDNA-PAINT. *Methods Mol Biol* 1663, 231-252.
- Beliveau, B.J., Joyce, E.F., Apostolopoulos, N., Yilmaz, F., Fonseka, C.Y., McCole, R.B., Chang, Y., Li, J.B., Senaratne, T.N., Williams, B.R., *et al.* (2012). Versatile design and synthesis platform for visualizing genomes with Oligopaint FISH probes. *Proceedings of the National Academy of Sciences of the United States of America* 109, 21301-21306.
- Beliveau, B.J., Kishi, J.Y., Nir, G., Sasaki, H.M., Saka, S.K., Nguyen, S.C., Wu, C.T., and Yin, P. (2018). OligoMiner provides a rapid, flexible environment for the design of genome-scale oligonucleotide in situ hybridization probes. *Proceedings of the National Academy of Sciences of the United States of America* 115, E2183-E2192.
- Benedetti, F., Drier, J., Burnier, Y., and Stasiak, A. (2014). Models that include supercoiling of topological domains reproduce several known features of interphase chromosomes. *Nucleic Acids Res* 42, 2848-2855.

Beringer, M., Pisano, P., Di Carlo, V., Blanco, E., Chammas, P., Vizan, P., Gutierrez, A., Aranda, S., Payer, B., Wierer, M., *et al.* (2016). EPOP Functionally Links Elongin and Polycomb in Pluripotent Stem Cells. *Molecular cell* **64**, 645-658.

Bermudez, I., Garcia-Martinez, J., Perez-Ortin, J.E., and Roca, J. (2010). A method for genome-wide analysis of DNA helical tension by means of psoralen-DNA photobinding. *Nucleic Acids Res* **38**, e182.

Bintu, B., Mateo, L.J., Su, J.-h., Sinnott-armstrong, N.A., Parker, M., Kinrot, S., Yamaya, K., Boettiger, A.N., and Zhuang, X. (2018). Super-resolution chromatin tracing reveals domains and cooperative interactions in single cells. *1783*.

Bjorkegren, C., and Baranello, L. (2018). DNA Supercoiling, Topoisomerases, and Cohesin: Partners in Regulating Chromatin Architecture? *Int J Mol Sci* **19**.

Boettiger, A.N., Bintu, B., Moffitt, J.R., Wang, S., Beliveau, B.J., Fudenberg, G., Imakaev, M., Mirny, L.A., Wu, C.T., and Zhuang, X. (2016). Super-resolution imaging reveals distinct chromatin folding for different epigenetic states. *Nature* **529**, 418-422.

Bray, N.L., Pimentel, H., Melsted, P., and Pachter, L. (2016). Near-optimal probabilistic RNA-seq quantification. *Nat Biotechnol* **34**, 525-527.

Busslinger, G.A., Stocsits, R.R., Van Der Lelij, P., Axelsson, E., Tedeschi, A., Galjart, N., and Peters, J.M. (2017). Cohesin is positioned in mammalian genomes by transcription, CTCF and Wapl. *Nature* **544**, 503-507.

Canela, A., Maman, Y., Huang, S.N., Wutz, G., Tang, W., Zagnoli-Vieira, G., Callen, E., Wong, N., Day, A., Peters, J.M., *et al.* (2019). Topoisomerase II-Induced Chromosome Breakage and Translocation Is Determined by Chromosome Architecture and Transcriptional Activity. *Molecular cell* **75**, 252-266 e258.

Canela, A., Maman, Y., Jung, S., Wong, N., Callen, E., Day, A., Kieffer-Kwon, K.-R., Pekowska, A., Zhang, H., Rao, S.S.P., *et al.* (2017). Genome Organization Drives Chromosome Fragility. *Cell* **170**, 507-521.e518.

Cardozo Gizzi, A.M., Cattoni, D.I., Fiche, J.B., Espinola, S.M., Gurgo, J., Messina, O., Houbon, C., Ogiyama, Y., Papadopoulos, G.L., Cavalli, G., *et al.* (2019). Microscopy-Based Chromosome Conformation Capture Enables Simultaneous Visualization of Genome Organization and Transcription in Intact Organisms. *Molecular cell* **74**, 212-222 e215.

Chen, J., Zhang, Z., Li, L., Chen, B.C., Revyakin, A., Hajj, B., Legant, W., Dahan, M., Lionnet, T., Betzig, E., *et al.* (2014). Single-molecule dynamics of enhanceosome assembly in embryonic stem cells. *Cell* **156**, 1274-1285.

Chen, S., Zhou, Y., Chen, Y., and Gu, J. (2018). fastp: an ultra-fast all-in-one FASTQ preprocessor. *Bioinformatics* **34**, i884-i890.

Davidson, I.F., Bauer, B., Goetz, D., Tang, W., Wutz, G., and Peters, J.M. (2019). DNA loop extrusion by human cohesin. *Science* **366**, 1338-1345.

Davidson, I.F., Goetz, D., Zaczek, M.P., Molodtsov, M.I., Huis in 't Veld, P.J., Weissmann, F., Litos, G., Cisneros, D.A., Ocampo- Hafalla, M., Ladurner, R., *et al.* (2016). Rapid movement and transcriptional re- localization of human cohesin on DNA. *The EMBO Journal* **35**, 2671-2685.

Dixon, J.R., Selvaraj, S., Yue, F., Kim, A., Li, Y., Shen, Y., Hu, M., Liu, J.S., and Ren, B. (2012). Topological domains in mammalian genomes identified by analysis of chromatin interactions. *Nature* **485**, 376-380.

Djebali, S., Davis, C.A., Merkel, A., Dobin, A., Lassmann, T., Mortazavi, A., Tanzer, A., Lagarde, J., Lin, W., Schlesinger, F., *et al.* (2012). Landscape of transcription in human cells. *Nature* **489**, 101-108.

Dobin, A., Davis, C.A., Schlesinger, F., Drenkow, J., Zaleski, C., Jha, S., Batut, P., Chaisson, M., and Gingeras, T.R. (2012). STAR: ultrafast universal RNA-seq aligner. *Bioinformatics* **29**, 15-21.

EncodeProjectConsortium (2012). An integrated encyclopedia of DNA elements in the human genome. *Nature* **489**, 57-74.

Fernandez, X., Diaz-Ingelmo, O., Martinez-Garcia, B., and Roca, J. (2014). Chromatin regulates DNA torsional energy via topoisomerase II-mediated relaxation of positive supercoils. *EMBO J* **33**, 1492-1501.

Fudenberg, G., Imakaev, M., Lu, C., Goloborodko, A., Abdennur, N., and Mirny, L.A. (2016). Formation of Chromosomal Domains by Loop Extrusion. *Cell Reports* **15**, 2038-2049.

Gassler, J., Brandão, H.B., Imakaev, M., Flyamer, I.M., Ladstätter, S., Bickmore, W.A., Peters, J.M., Mirny, L.A., and Tachibana, K. (2017). A mechanism of cohesin- dependent loop extrusion organizes zygotic genome architecture. *The EMBO Journal*, e201798083.

Gilbert, N., and Allan, J. (2014). Supercoiling in DNA and chromatin. *Current opinion in genetics & development* **25**, 15-21.

Gothé, H.J., Bouwman, B.A.M., Gusmao, E.G., Piccinno, R., Petrosino, G., Sayols, S., Drechsel, O., Minneker, V., Josipovic, N., Mizi, A., *et al.* (2019). Spatial Chromosome Folding and Active Transcription Drive DNA Fragility and Formation of Oncogenic MLL Translocations. *Molecular cell* **75**, 267-283 e212.

Grimm, J.B., English, B.P., Chen, J., Slaughter, J.P., Zhang, Z., Revyakin, A., Patel, R., Macklin, J.J., Normanno, D., Singer, R.H., *et al.* (2015). A general method to improve fluorophores for live-cell and single-molecule microscopy. *Nature Methods* **12**, 244-250.

Grubert, F., Srivas, R., Spacek, D.V., Kasowski, M., Ruiz-Velasco, M., Sinnott-Armstrong, N., Greenside, P., Narasimha, A., Liu, Q., Geller, B., *et al.* (2020). Landscape of cohesin-mediated chromatin loops in the human genome. *Nature* **583**, 737-743.

Haarhuis, J.H.I., van der Weide, R.H., Blomen, V.A., Yanez-Cuna, J.O., Amendola, M., van Ruiten, M.S., Krijger, P.H.L., Teunissen, H., Medema, R.H., van Steensel, B., *et al.* (2017). The Cohesin Release Factor WAPL Restricts Chromatin Loop Extension. *Cell* **169**, 693-707 e614.

Hangauer, M.J., Vaughn, I.W., and McManus, M.T. (2013). Pervasive transcription of the human genome produces thousands of previously unidentified long intergenic noncoding RNAs. *PLoS Genet* **9**, e1003569.

Hansen, A.S., Pustova, I., Cattoglio, C., Tjian, R., and Darzacq, X. (2017). CTCF and cohesin regulate chromatin loop stability with distinct dynamics. *eLife* **6**.

Hassler, M., Shaltiel, I.A., and Haering, C.H. (2018). Towards a Unified Model of SMC Complex Function. *Current biology : CB* **28**, R1266-R1281.

Hilbert, L., Sato, Y., Kuznetsova, K., Bianucci, T., Kimura, H., Julicher, F., Honigsmann, A., Zaburdaev, V., and Vastenhouw, N.L. (2021). Transcription organizes euchromatin via microphase separation. *Nat Commun* **12**, 1360.

Huang, B., Wang, W., Bates, M., and Zhuang, X. (2008). Three-dimensional super-resolution imaging by stochastic optical reconstruction microscopy. *Science* 319, 810-813.

Hug, C.B., Grimaldi, A.G., Kruse, K., and Vaquerizas, J.M. (2017). Chromatin Architecture Emerges during Zygotic Genome Activation Independent of Transcription. *Cell* 169, 216-228 e219.

Joshi, R.S., Pina, B., and Roca, J. (2012). Topoisomerase II is required for the production of long Pol II gene transcripts in yeast. *Nucleic Acids Res* 40, 7907-7915.

Kagey, M.H., Newman, J.J., Bilodeau, S., Zhan, Y., Orlando, D.A., van Berkum, N.L., Ebmeier, C.C., Goossens, J., Rahl, P.B., Levine, S.S., *et al.* (2010). Mediator and cohesin connect gene expression and chromatin architecture. *Nature* 467, 430-435.

Kim, T.K., Hemberg, M., Gray, J.M., Costa, A.M., Bear, D.M., Wu, J., Harmin, D.A., Laptewicz, M., Barbara-Haley, K., Kuersten, S., *et al.* (2010). Widespread transcription at neuronal activity-regulated enhancers. *Nature* 465, 182-187.

Kim, Y., Shi, Z., Zhang, H., Finkelstein, I.J., and Yu, H. (2019). Human cohesin compacts DNA by loop extrusion. *Science* 366, 1345-1349.

Kim, Y.W., Lee, S., Yun, J., and Kim, A. (2015). Chromatin looping and eRNA transcription precede the transcriptional activation of gene in the beta-globin locus. *Biosci Rep* 35.

Kouzine, F., Gupta, A., Baranello, L., Wojtowicz, D., Ben-Aissa, K., Liu, J., Przytycka, T.M., and Levens, D. (2013). Transcription-dependent dynamic supercoiling is a short-range genomic force. *Nat Struct Mol Biol* 20, 396-403.

Kramer, P.R., Bat, O., and Sinden, R.R. (1999). Measurement of localized DNA supercoiling and topological domain size in eukaryotic cells. *Methods Enzymol* 304, 639-650.

Kramer, P.R., and Sinden, R.R. (1997). Measurement of unrestrained negative supercoiling and topological domain size in living human cells. *Biochemistry* 36, 3151-3158.

Krietenstein, N., Abraham, S., Venev, S.V., Abdennur, N., Gibcus, J., Hsieh, T.S., Parsi, K.M., Yang, L., Maehr, R., Mirny, L.A., *et al.* (2020). Ultrastructural Details of Mammalian Chromosome Architecture. *Molecular cell* 78, 554-565 e557.

Kueng, S., Hegemann, B., Peters, B.H., Lipp, J.J., Schleiffer, A., Mechtler, K., and Peters, J.M. (2006). Wapl Controls the Dynamic Association of Cohesin with Chromatin. *Cell* 127, 955-967.

Lakadamyali, M., and Cosma, M.P. (2020). Visualizing the genome in high resolution challenges our textbook understanding. *Nat Methods* 17, 371-379.

Le, T.B., Imakaev, M.V., Mirny, L.A., and Laub, M.T. (2013). High-resolution mapping of the spatial organization of a bacterial chromosome. *Science* 342, 731-734.

Lengronne, A., Katou, Y., Mori, S., Yokobayashi, S., Kelly, G.P., Itoh, T., Watanabe, Y., Shirahige, K., and Uhlmann, F. (2004). Cohesin relocation from sites of chromosomal loading to places of convergent transcription. *Nature* 430, 573-578.

Levet, F., Hosy, E., Kechkar, A., Butler, C., Beghin, A., Choquet, D., and Sibarita, J.B. (2015). SR-Tesseler: A method to segment and quantify localization-based super-resolution microscopy data. *Nature Methods* 12, 1065-1071.

Li, L., Lyu, X., Hou, C., Takenaka, N., Nguyen, H.Q., Ong, C.T., Cubenas-Potts, C., Hu, M., Lei, E.P., Bosco, G., *et al.* (2015). Widespread rearrangement of 3D chromatin organization underlies polycomb-mediated stress-induced silencing. *Molecular cell* 58, 216-231.

Ljungman, M., and Hanawalt, P.C. (1992). Localized torsional tension in the DNA of human cells. *Proceedings of the National Academy of Sciences of the United States of America* 89, 6055-6059.

Ljungman, M., and Hanawalt, P.C. (1995). Presence of negative torsional tension in the promoter region of the transcriptionally poised dihydrofolate reductase gene in vivo. *Nucleic Acids Res* 23, 1782-1789.

Marinov, G.K., Trevino, A.E., Xiang, T., Kundaje, A., Grossman, A.R., and Greenleaf, W.J. (2020). Transcription-dependent domain-scale 3D genome organization in dinoflagellates. *bioRxiv*, 2020.2007.2001.181685.

Mateo, L.J., Murphy, S.E., Hafner, A., Cinquini, I.S., Walker, C.A., and Boettiger, A.N. (2019). Visualizing DNA folding and RNA in embryos at single-cell resolution. *Nature* 568, 49-54.

Matsumoto, K., and Hirose, S. (2004). Visualization of unconstrained negative supercoils of DNA on polytene chromosomes of *Drosophila*. *J Cell Sci* 117, 3797-3805.

Mazza, D., Abernathy, A., Golob, N., Morisaki, T., and McNally, J.G. (2012). A benchmark for chromatin binding measurements in live cells. *Nucleic Acids Res* 40, e119.

McCord, R.P., Kaplan, N., and Giorgetti, L. (2020). Chromosome Conformation Capture and Beyond: Toward an Integrative View of Chromosome Structure and Function. *Molecular cell* 77, 688-708.

Nagashima, R., Hibino, K., Ashwin, S.S., Babokhov, M., Fujishiro, S., Imai, R., Nozaki, T., and Tamura, S. (2019). Single nucleosome imaging reveals loose genome chromatin networks via active RNA polymerase II.

Nasmyth, K. (2001). Disseminating the Genome: Joining, Resolving, and Separating Sister Chromatids During Mitosis and Meiosis. *Annual Review of Genetics* 35, 673-745.

Nativio, R., Wendt, K.S., Ito, Y., Huddleston, J.E., Uribe-Lewis, S., Woodfine, K., Krueger, C., Reik, W., Peters, J.M., and Murrell, A. (2009). Cohesin is required for higher-order chromatin conformation at the imprinted IGF2-H19 locus. *PLoS Genetics* 5.

Naughton, C., Avlonitis, N., Corless, S., Prendergast, J.G., Mati, I.K., Eijk, P.P., Cockroft, S.L., Bradley, M., Ylstra, B., and Gilbert, N. (2013). Transcription forms and remodels supercoiling domains unfolding large-scale chromatin structures. *Nature Structural and Molecular Biology* 20, 387-395.

Neguembor, M.V., Xynos, A., Onorati, M.C., Caccia, R., Bortolanza, S., Godio, C., Pistoni, M., Corona, D.F., Schotta, G., and Gabellini, D. (2013). FSHD muscular dystrophy region gene 1 binds Suv4-20h1 histone methyltransferase and impairs myogenesis. *J Mol Cell Biol* 5, 294-307.

Nguyen, H.Q., Chatteraj, S., Castillo, D., Nguyen, S.C., Nir, G., Lioutas, A., Hershberg, E.A., Martins, N.M.C., Reginato, P.L., Hannan, M., *et al.* (2020). 3D mapping and accelerated super-resolution imaging of the human genome using in situ sequencing. *Nat Methods* 17, 822-832.

Nir, G., Farabella, I., Perez Estrada, C., Ebeling, C.G., Beliveau, B.J., Sasaki, H.M., Lee, S.D., Nguyen, S.C., McCole, R.B., Chatteraj, S., *et al.* (2018). Walking along chromosomes with super-resolution imaging, contact maps, and integrative modeling. *PLoS Genet* 14, e1007872.

Nora, E.P., Lajoie, B.R., Schulz, E.G., Giorgetti, L., Okamoto, I., Servant, N., Piolot, T., van Berkum, N.L., Meisig, J., Sedat, J., *et al.* (2012). Spatial partitioning of the regulatory landscape of the X-inactivation centre. *Nature* 485, 381-385.

Nuebler, J., Fudenberg, G., Imakaev, M., Abdennur, N., and Mirny, L.A. (2018). Chromatin organization by an interplay of loop extrusion and compartmental segregation. *Proceedings of the National Academy of Sciences* 115, E6697-E6706.

Ocampo-Hafalla, M., Munoz, S., Samora, C.P., and Uhlmann, F. (2016). Evidence for cohesin sliding along budding yeast chromosomes. *Open Biol* 6.

Olan, I., Parry, A.J., Schoenfelder, S., Narita, M., Ito, Y., Chan, A.S.L., Slater, G.S.C., Bihary, D., Bando, M., Shirahige, K., *et al.* (2019). Transcription-driven cohesin repositioning rewires chromatin loops in cellular senescence. *bioRxiv*, 823831.

Orlandini, E., Marenduzzo, D., and Michieletto, D. (2019). Synergy of topoisomerase and structural-maintenance-of-chromosomes proteins creates a universal pathway to simplify genome topology. *Proceedings of the National Academy of Sciences of the United States of America* 116, 8149-8154.

Otterstrom, J., Castells-Garcia, A., Vicario, C., Gomez-Garcia, P.A., Cosma, M.P., and Lakadamyali, M. (2019). Super-resolution microscopy reveals how histone tail acetylation affects DNA compaction within nucleosomes in vivo. *Nucleic Acids Res* 47, 8470-8484.

Parelho, V., Hadjur, S., Spivakov, M., Leleu, M., Sauer, S., Gregson, H.C., Jarmuz, A., Canzonetta, C., Webster, Z., Nesterova, T., *et al.* (2008). Cohesins functionally associate with CTCF on mammalian chromosome arms. *Cell* 132, 422-433.

Perry, R.P., and Kelley, D.E. (1970). Inhibition of RNA synthesis by actinomycin D: characteristic dose-response of different RNA species. *J Cell Physiol* 76, 127-139.

Pommier, Y., Leo, E., Zhang, H., and Marchand, C. (2010). DNA topoisomerases and their poisoning by anticancer and antibacterial drugs. *Chem Biol* 17, 421-433.

Pommier, Y., Sun, Y., Huang, S.N., and Nitiss, J.L. (2016). Roles of eukaryotic topoisomerases in transcription, replication and genomic stability. *Nat Rev Mol Cell Biol* 17, 703-721.

Postow, L., Hardy, C.D., Arsuaga, J., and Cozzarelli, N.R. (2004). Topological domain structure of the Escherichia coli chromosome. *Genes & development* 18, 1766-1779.

Racko, D., Benedetti, F., Dorier, J., and Stasiak, A. (2018). Transcription-induced supercoiling as the driving force of chromatin loop extrusion during formation of TADs in interphase chromosomes. *Nucleic Acids Research* 46, 1648-1660.

Racko, D., Benedetti, F., Dorier, J., and Stasiak, A. (2019). Are TADs supercoiled? *Nucleic acids research* 47, 521-532.

Ran, F.A., Hsu, P.D., Wright, J., Agarwala, V., Scott, D.A., and Zhang, F. (2013). Genome engineering using the CRISPR-Cas9 system. *Nat Protoc* 8, 2281-2308.

Rao, S.S., Huntley, M.H., Durand, N.C., Stamenova, E.K., Bochkov, I.D., Robinson, J.T., Sanborn, A.L., Machol, I., Omer, A.D., Lander, E.S., *et al.* (2014). A 3D map of the human genome at kilobase resolution reveals principles of chromatin looping. *Cell* 159, 1665-1680.

Rao, S.S.P., Huang, S.-c., Glenn, B., Hilaire, S., Engreitz, J.M., Perez, E.M., Sanborn, A.L., Sarah, E., Bascom, G.D., Bochkov, I.D., *et al.* (2017). Cohesin loss eliminates all loop domains. *Cell* 171, 305-320.

RCoreTeam (2014). R: A Language and Environment for Statistical Computing.

Rhodes, J., Mazza, D., Nasmyth, K., and Uphoff, S. (2017a). Scc2/Nipbl hops between chromosomal cohesin rings after loading. *eLife* 6, 1-20.

Rhodes, J.D.P., Haarhuis, J.H.I., Grimm, J.B., Rowland, B.D., Lavis, L.D., and Nasmyth, K.A. (2017b). Cohesin Can Remain Associated with Chromosomes during DNA Replication. *Cell Rep* 20, 2749-2755.

Ricci, M.A., Manzo, C., Garcia-Parajo, M.F., Lakadamyali, M., and Cosma, M.P. (2015). Chromatin fibers are formed by heterogeneous groups of nucleosomes in vivo. *Cell* 160, 1145-1158.

Rowley, M.J., and Corces, V.G. (2018). Organizational principles of 3D genome architecture. *Nature reviews. Genetics* 19, 789-800.

Rowley, M.J., Lyu, X., Rana, V., Ando-kuri, M., and Karns, R. (2019). Condensin II Counteracts Cohesin and RNA Polymerase II in the Establishment of 3D Chromatin Organization. *CellReports* 26, 2890-2903.e2893.

Rueden, C.T., Schindelin, J., Hiner, M.C., DeZonia, B.E., Walter, A.E., Arena, E.T., and Eliceiri, K.W. (2017). ImageJ2: ImageJ for the next generation of scientific image data. *BMC Bioinformatics* 18, 529.

Ruskova, R., and Racko, D. (2021). Entropic Competition between Supercoiled and Torsionally Relaxed Chromatin Fibers Drives Loop Extrusion through Pseudo-Topologically Bound Cohesin. *Biology (Basel)* 10.

Rust, M.J., Bates, M., and Zhuang, X. (2006). Sub-diffraction-limit imaging by stochastic optical reconstruction microscopy (STORM). *Nat Methods* 3, 793-795.

Saksouk, N., Simboeck, E., and Dejardin, J. (2015). Constitutive heterochromatin formation and transcription in mammals. *Epigenetics Chromatin* 8, 3.

Saldana-Meyer, R., Rodriguez-Hernaez, J., Escobar, T., Nishana, M., Jacome-Lopez, K., Nora, E.P., Bruneau, B.G., Tsirigos, A., Furlan-Magaril, M., Skok, J., *et al.* (2019). RNA Interactions Are Essential for CTCF-Mediated Genome Organization. *Molecular cell* 76, 412-422 e415.

Sanborn, A.L., Rao, S.S.P., Huang, S.-C., Durand, N.C., Huntley, M.H., Jewett, A.I., Bochkov, I.D., Chinnappan, D., Cutkosky, A., Li, J., *et al.* (2015). Chromatin extrusion explains key features of loop and domain formation in wild-type and engineered genomes. *Proceedings of the National Academy of Sciences* 112, E6456-E6465.

Schwarzer, W., Abdennur, N., Goloborodko, A., Pekowska, A., Fudenberg, G., Loe-Mie, Y., Fonseca, N.A., Huber, W., Haering, C.H., Mirny, L., *et al.* (2017). Two independent modes of chromatin organization revealed by cohesin removal. *Nature* 551, 51-56.

Sexton, T., Yaffe, E., Kenigsberg, E., Bantignies, F., Leblanc, B., Hoichman, M., Parrinello, H., Tanay, A., and Cavalli, G. (2012). Three-dimensional folding and functional organization principles of the *Drosophila* genome. *Cell* **148**, 458-472.

Shivanandan, A., Unnikrishnan, J., and Radenovic, A. (2016). On characterizing protein spatial clusters with correlation approaches. *Sci Rep* **6**, 31164.

Sinden, R.R., Carlson, J.O., and Pettijohn, D.E. (1980). Torsional tension in the DNA double helix measured with trimethylpsoralen in living *E. coli* cells: analogous measurements in insect and human cells. *Cell* **21**, 773-783.

Stigler, J., Camdere, G.O., Koshland, D.E., and Greene, E.C. (2016). Single-Molecule Imaging Reveals a Collapsed Conformational State for DNA-Bound Cohesin. *Cell Rep* **15**, 988-998.

Su, J.H., Zheng, P., Kinrot, S.S., Bintu, B., and Zhuang, X. (2020). Genome-Scale Imaging of the 3D Organization and Transcriptional Activity of Chromatin. *Cell* **182**, 1641-1659 e1626.

Sutani, T., Kawaguchi, T., Kanno, R., Itoh, T., and Shirahige, K. (2009). Budding yeast Wpl1(Rad61)-Pds5 complex counteracts sister chromatid cohesion-establishing reaction. *Current biology : CB* **19**, 492-497.

Tarantino, N., Tinevez, J.Y., Crowell, E.F., Boisson, B., Henriques, R., Mhlanga, M., Agou, F., Israel, A., and Laplantine, E. (2014). TNF and IL-1 exhibit distinct ubiquitin requirements for inducing NEMO-IKK supramolecular structures. *The Journal of cell biology* **204**, 231-245.

Tedeschi, A., Wutz, G., Huet, S., Jaritz, M., Wuensche, A., Schirghuber, E., Davidson, I.F., Tang, W., Cisneros, D.A., Bhaskara, V., *et al.* (2013). Wapl is an essential regulator of chromatin structure and chromosome segregation. *Nature* **501**, 564-568.

Tinevez, J.Y., Perry, N., Schindelin, J., Hoopes, G.M., Reynolds, G.D., Laplantine, E., Bednarek, S.Y., Shorte, S.L., and Eliceiri, K.W. (2017). TrackMate: An open and extensible platform for single-particle tracking. *Methods* **115**, 80-90.

Tran, N.T., Laub, M.T., and Le, T.B.K. (2017). SMC Progressively Aligns Chromosomal Arms in *Caulobacter crescentus* but Is Antagonized by Convergent Transcription. *Cell Rep* **20**, 2057-2071.

Uuskula-Reimand, L., Hou, H., Samavarchi-Tehrani, P., Rudan, M.V., Liang, M., Medina-Rivera, A., Mohammed, H., Schmidt, D., Schwalie, P., Young, E.J., *et al.* (2016). Topoisomerase II beta interacts with cohesin and CTCF at topological domain borders. *Genome Biol* **17**, 182.

Valdes, A., Coronel, L., Martinez-Garcia, B., Segura, J., Dyson, S., Diaz-Ingelmo, O., Micheletti, C., and Roca, J. (2019). Transcriptional supercoiling boosts topoisomerase II-mediated knotting of intracellular DNA. *Nucleic Acids Res* **47**, 6946-6955.

Valdes, A., Segura, J., Dyson, S., Martinez-Garcia, B., and Roca, J. (2018). DNA knots occur in intracellular chromatin. *Nucleic Acids Res* **46**, 650-660.

van Steensel, B., and Furlong, E.E.M. (2019). The role of transcription in shaping the spatial organization of the genome. *Nat Rev Mol Cell Biol* **20**, 327-337.

Vian, L., Pekowska, A., Rao, S.S.P., Kieffer-Kwon, K.R., Jung, S., Baranello, L., Huang, S.C., El Khattabi, L., Dose, M., Pruett, N., *et al.* (2018). The Energetics and Physiological Impact of Cohesin Extrusion. *Cell* **175**, 292-294.

Vietri Rudan, M., Barrington, C., Henderson, S., Ernst, C., Odom, D.T., Tanay, A., and Hadjur, S. (2015). Comparative Hi-C Reveals that CTCF Underlies Evolution of Chromosomal Domain Architecture. *Cell Reports* 10, 1297-1309.

Wang, X., Brandao, H.B., Le, T.B., Laub, M.T., and Rudner, D.Z. (2017). *Bacillus subtilis* SMC complexes juxtapose chromosome arms as they travel from origin to terminus. *Science* 355, 524-527.

Watrén, E., Schleiffer, A., Tanaka, K., Eisenhaber, F., Nasmyth, K., and Peters, J.M. (2006). Human Scc4 is required for cohesin binding to chromatin, sister-chromatid cohesion, and mitotic progression. *Current biology : CB* 16, 863-874.

Wendt, K.S., Yoshida, K., Itoh, T., Bando, M., Koch, B., Schirghuber, E., Tsutsumi, S., Nagae, G., Ishihara, K., Mishiro, T., *et al.* (2008). Cohesin mediates transcriptional insulation by CCCTC-binding factor. *Nature* 451, 796-801.

Wieser, S., and Schutz, G.J. (2008). Tracking single molecules in the live cell plasma membrane-Do's and Don't's. *Methods* 46, 131-140.

Wutz, G., Várnai, C., Nagasaka, K., Cisneros, D.A., Stocsits, R.R., Tang, W., Schoenfelder, S., Jessberger, G., Muhar, M., Hossain, M.J., *et al.* (2017). Topologically associating domains and chromatin loops depend on cohesin and are regulated by CTCF, WAPL, and PDS5 proteins. *The EMBO Journal* 36, 3573-3599.

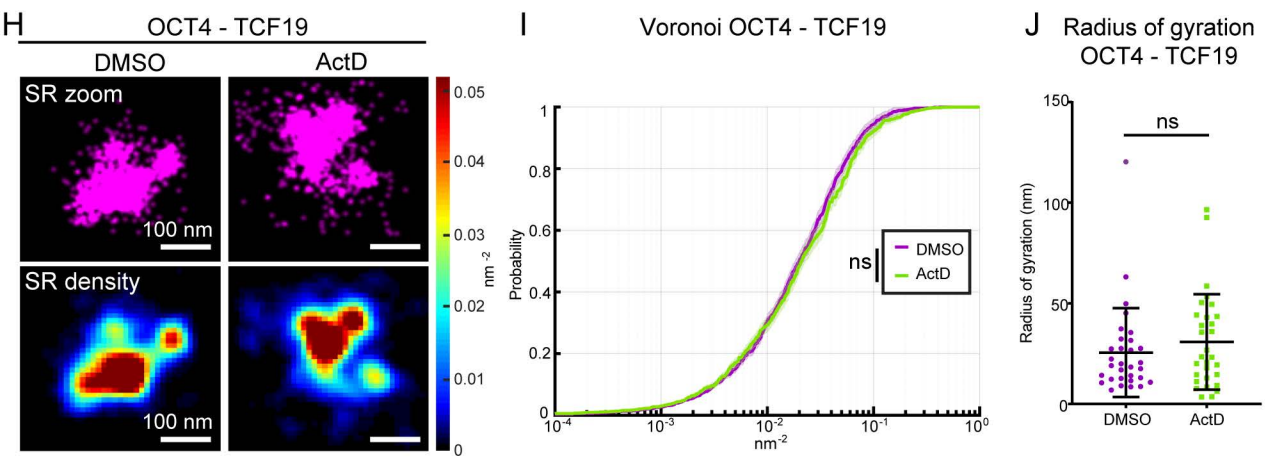
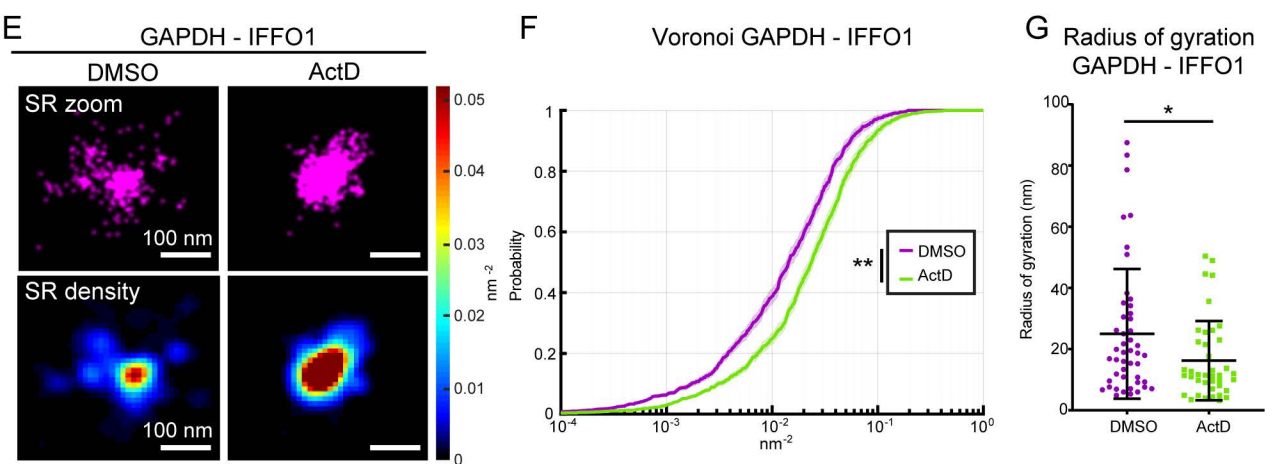
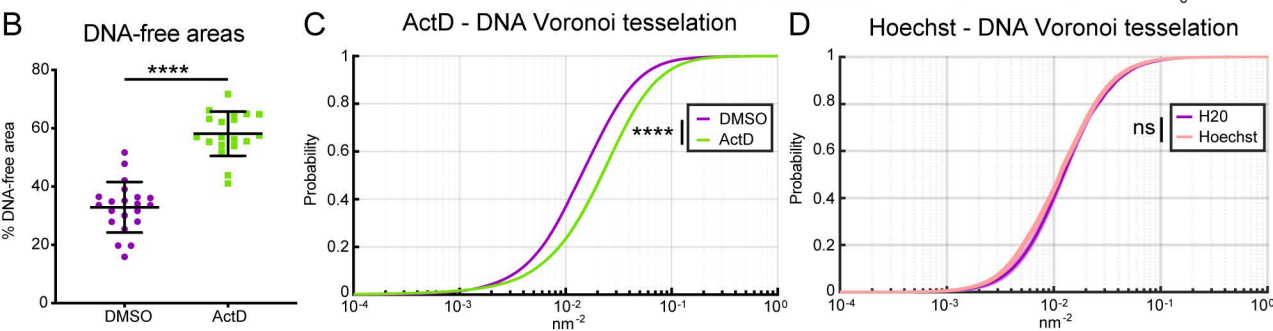
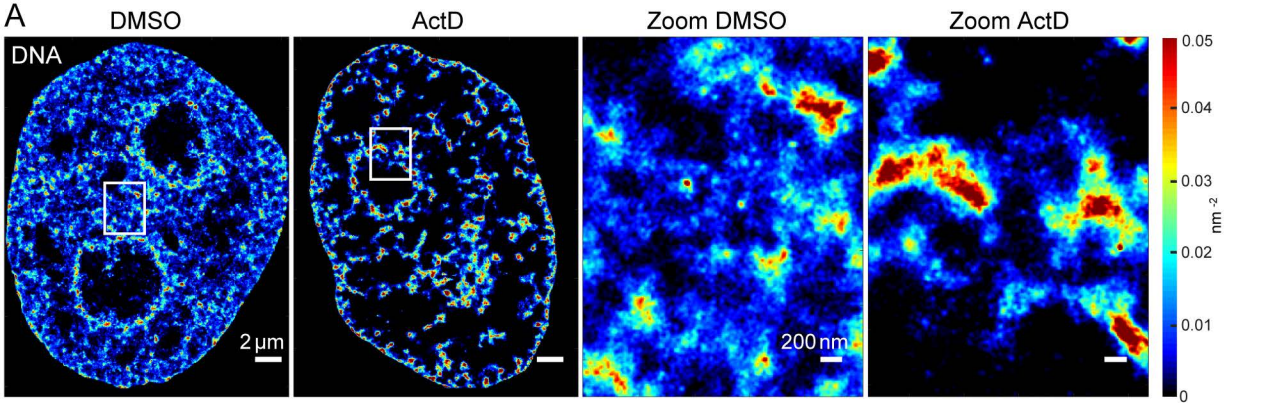
Yan, Y., Ding, Y., Leng, F., Dunlap, D., and Finzi, L. (2018). Protein-mediated loops in supercoiled DNA create large topological domains. *Nucleic Acids Res* 46, 4417-4424.

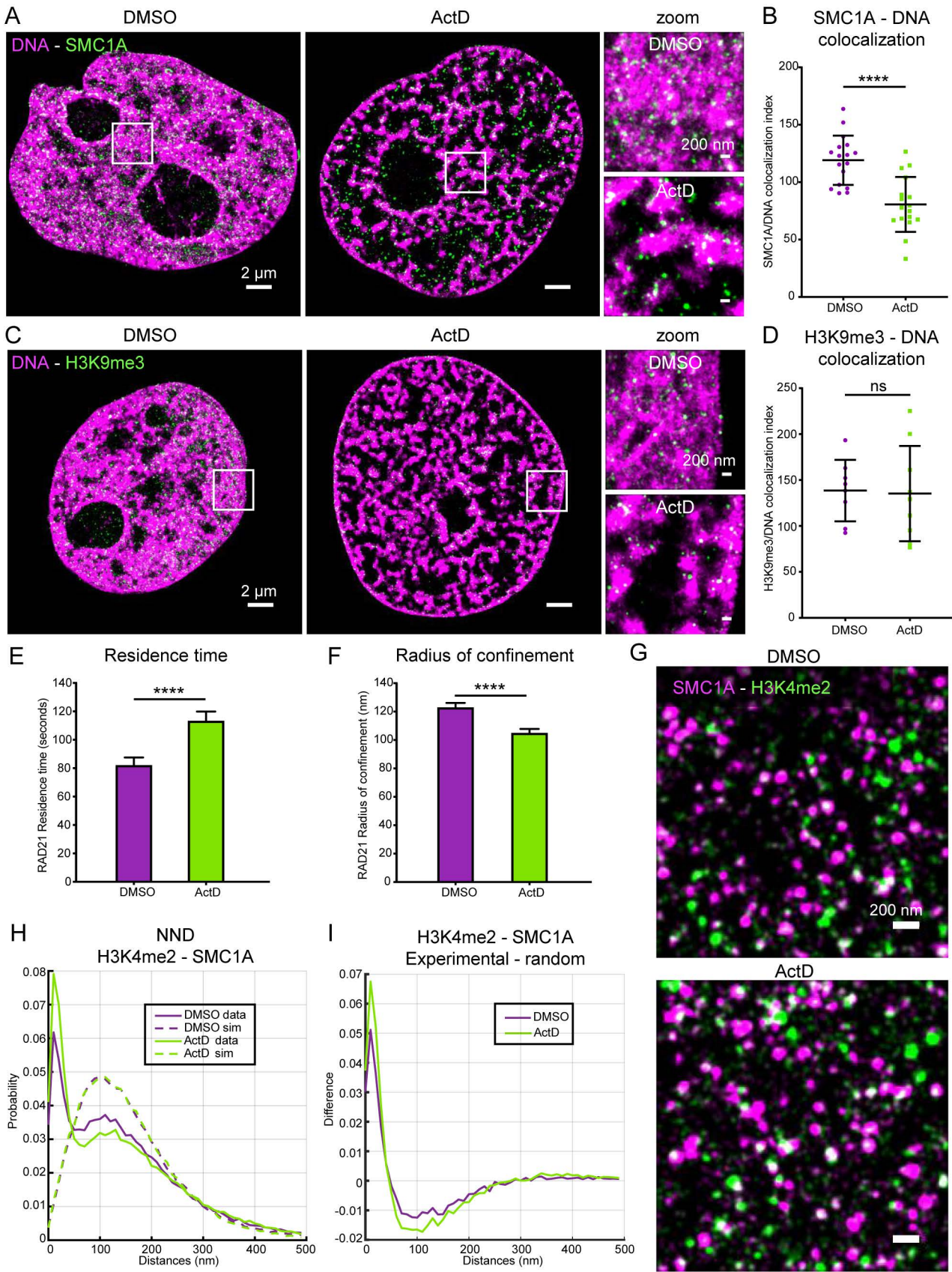
Yu, G., Wang, L.G., and He, Q.Y. (2015). ChIPseeker: an R/Bioconductor package for ChIP peak annotation, comparison and visualization. *Bioinformatics* 31, 2382-2383.

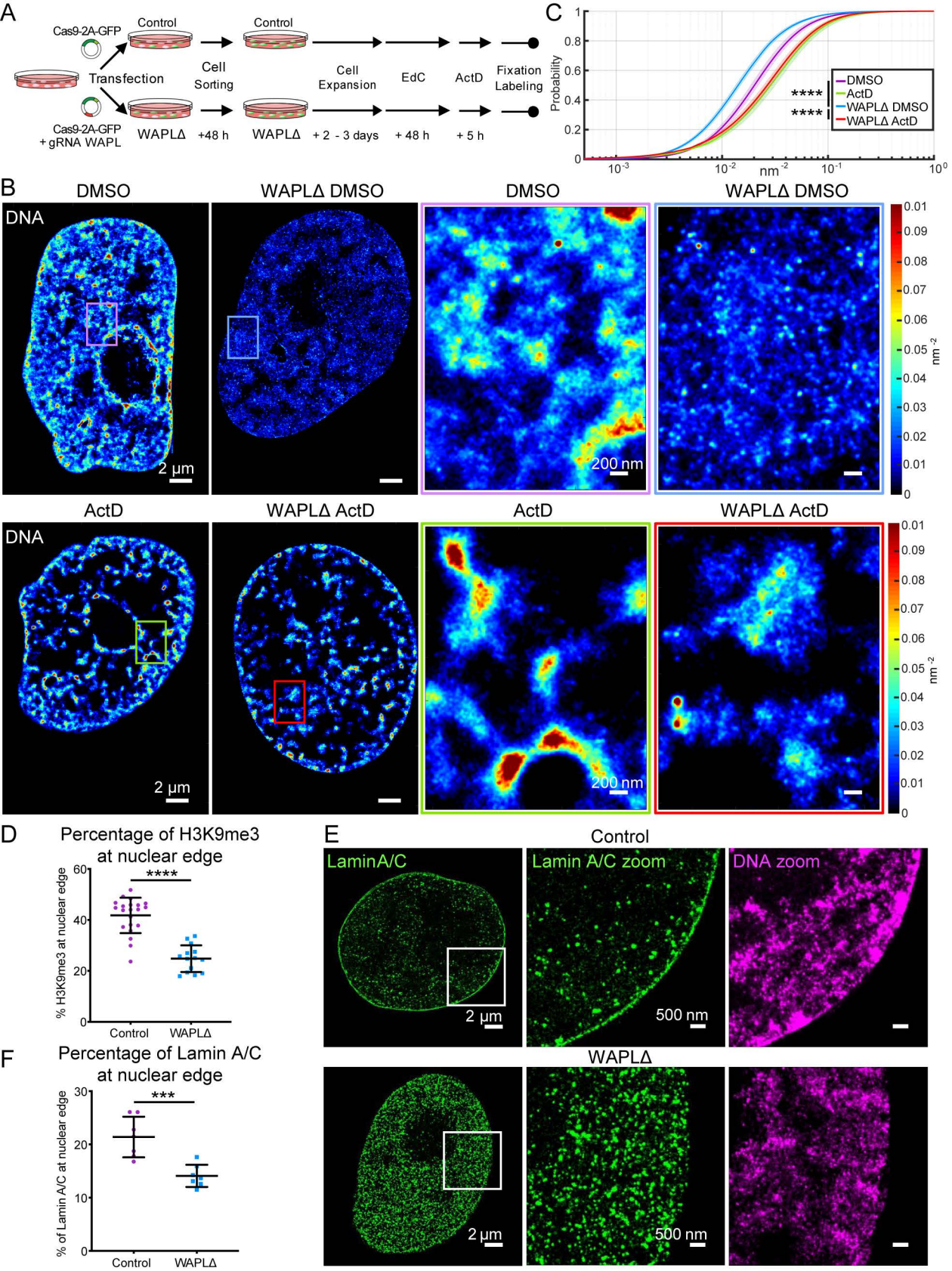
Zanacchi, F.C., Manzo, C., Alvarez, A.S., Derr, N.D., Garcia-Parajo, M.F., and Lakadamyali, M. (2017). A DNA origami platform for quantifying protein copy number in super-resolution. *Nat Methods* 14, 789-792.

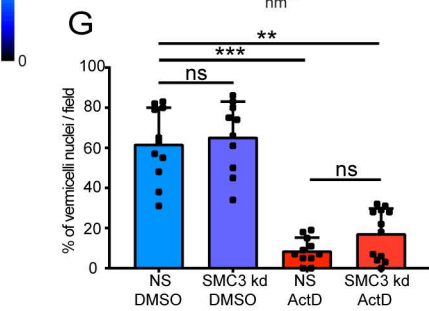
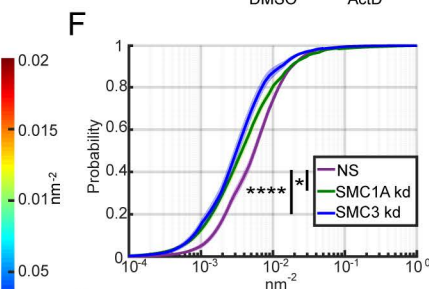
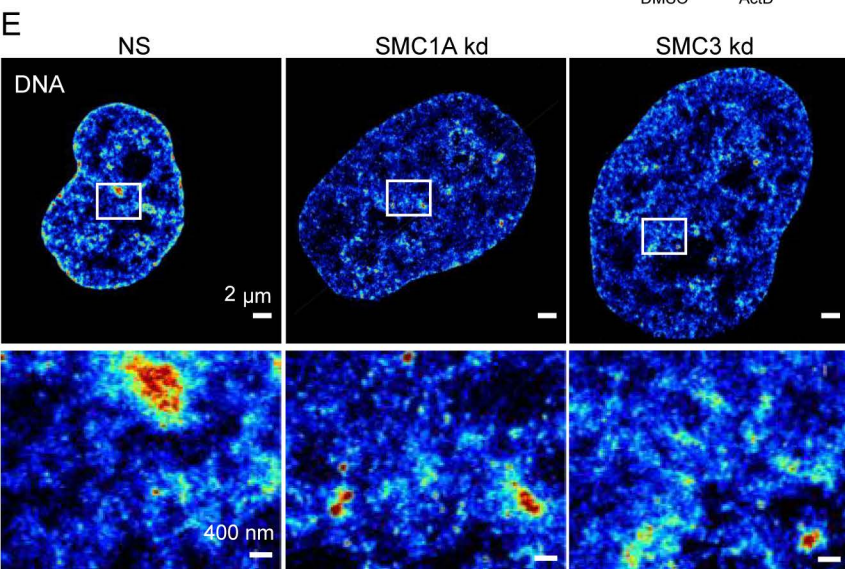
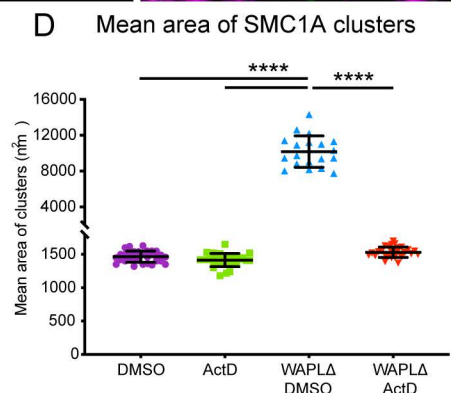
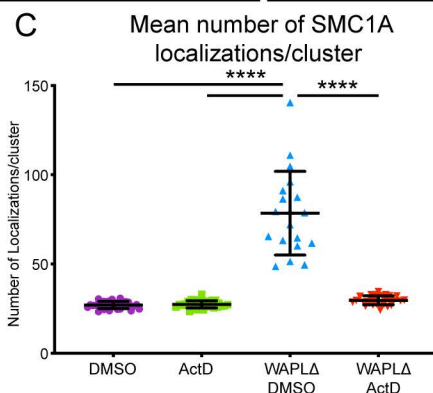
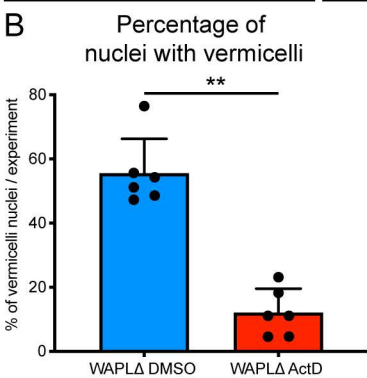
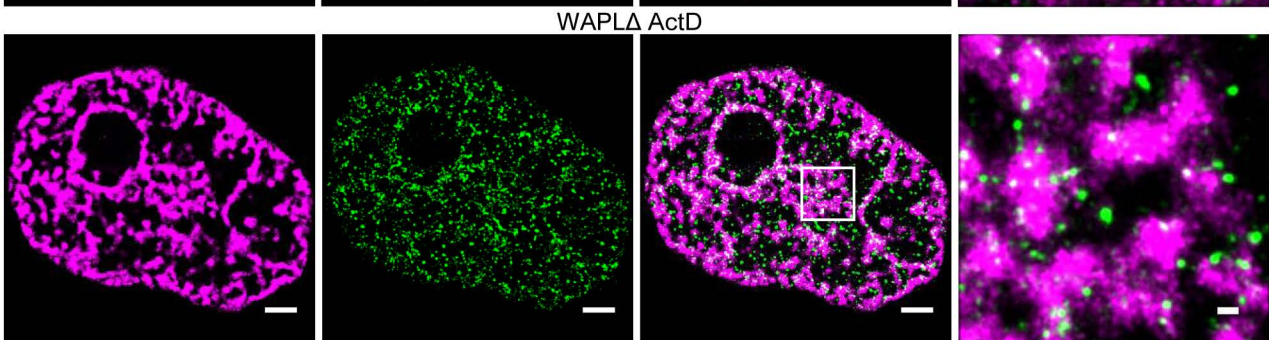
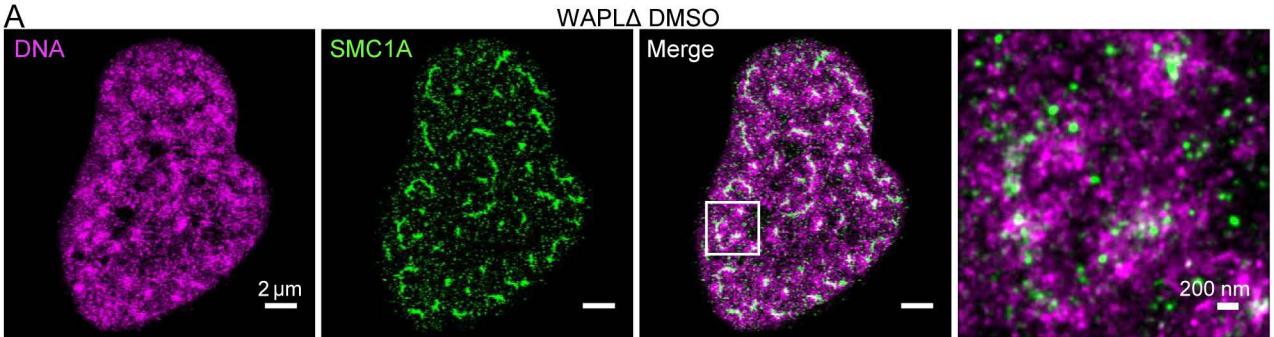
Zhang, Y., Liu, T., Meyer, C.A., Eeckhoute, J., Johnson, D.S., Bernstein, B.E., Nusbaum, C., Myers, R.M., Brown, M., Li, W., *et al.* (2008). Model-based analysis of ChIP-Seq (MACS). *Genome Biol* 9, R137.

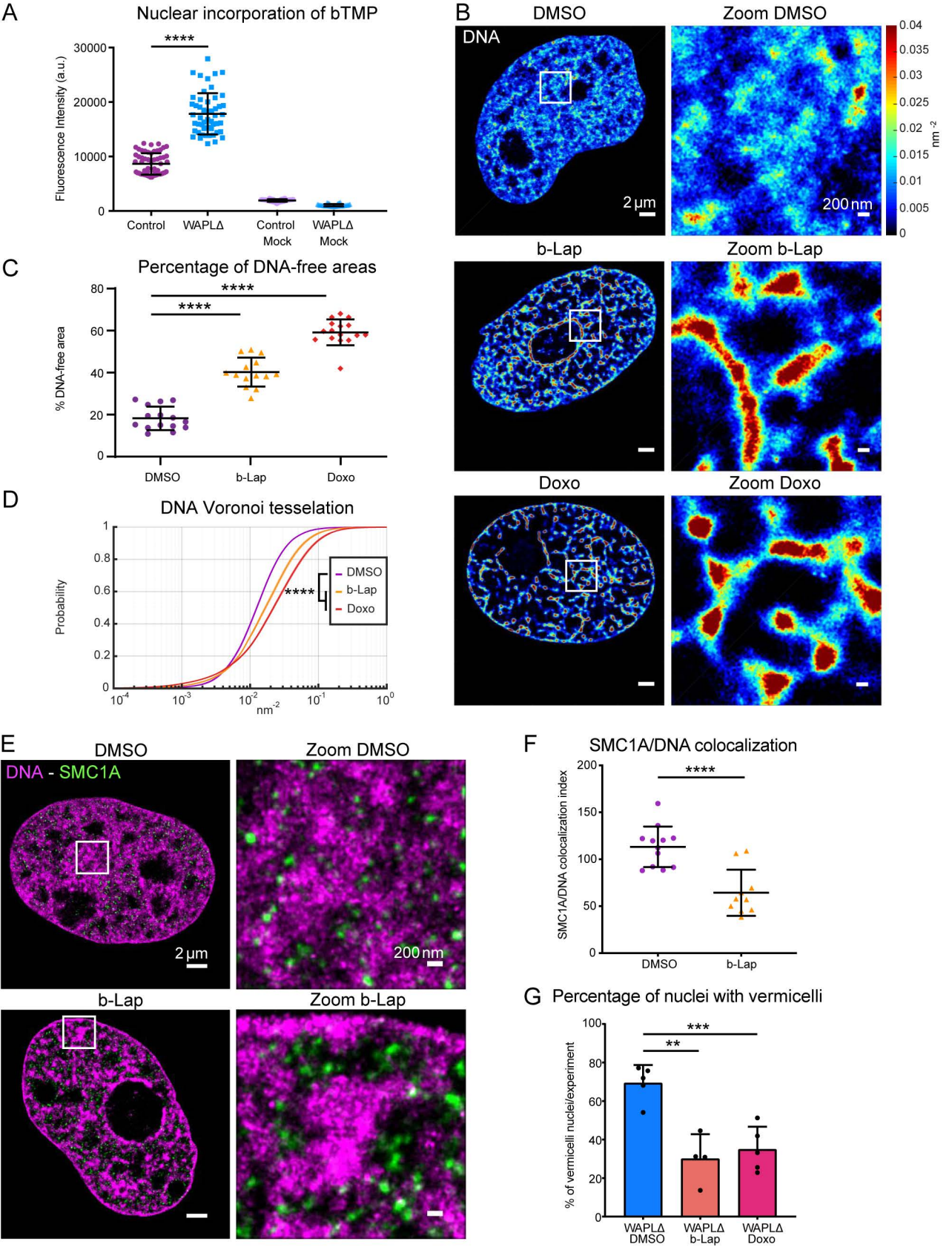
Zuin, J., Franke, V., van IJcken, W.F.J., van der Sloot, A., Krantz, I.D., van der Reijden, M.I.J.A., Nakato, R., Lenhard, B., and Wendt, K.S. (2014). A Cohesin-Independent Role for NIPBL at Promoters Provides Insights in CdLS. *PLoS Genetics* 10.



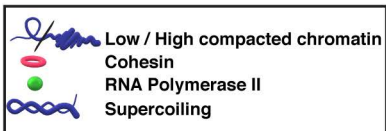
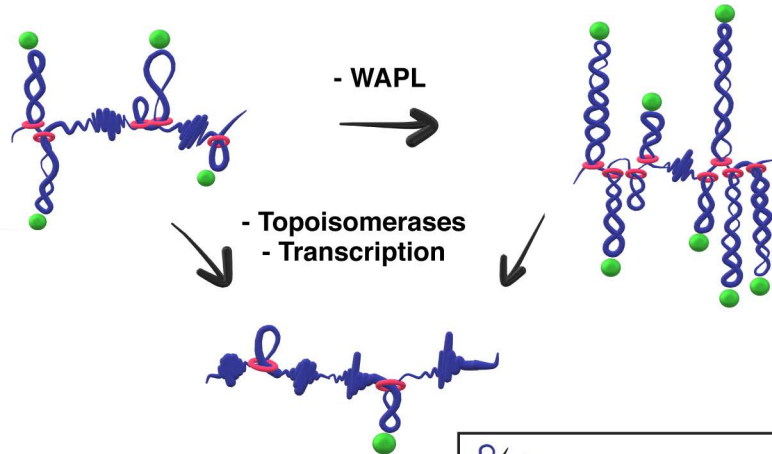








Chromatin blending



SUPPLEMENTAL INFORMATION

Transcription-mediated supercoiling regulates genome folding and loop formation

Maria Victoria Neguembor, Laura Martin, Álvaro Castells-García, Pablo Aurelio Gómez-García, Chiara Vicario, Davide Carnevali, Jumana AlHaj Abed, Alba Granados, Ruben Sebastian-Perez, Francesco Sottile, Jérôme Solon, Chao-ting Wu, Melike Lakadamyali and Maria Pia Cosma.

SUPPLEMENTAL FIGURES and LEGENDS (Pages 2 to 15)

SUPPLEMENTAL TABLES and LEGENDS (Pages 16 to 21)

SUPPLEMENTAL FIGURES and LEGENDS

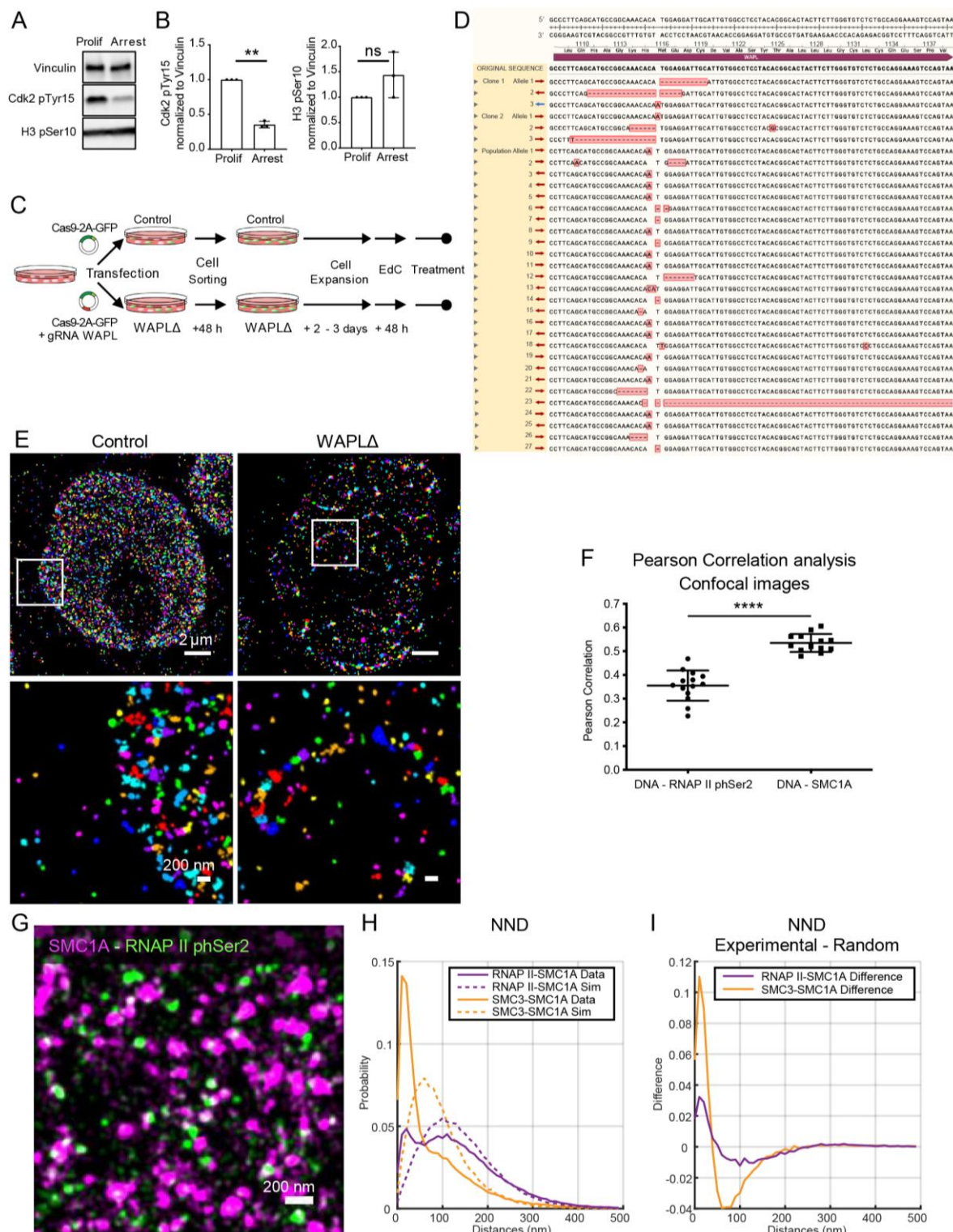


Figure S1. Experimental system and characterization of WAPLΔ cells, related to Figure 1

- A. Representative Western Blots for proliferative (Prolif) and serum starved (Arrest) HeLa cells. Vinculin, Cdk2 phospho Tyr15 (Cdk2 pTyr15) and Histone H3 phospho Ser10 (H3 pSer10) blots are shown.
- B. Western Blot quantification of Cdk2 phospho Tyr15 (Cdk2 pTyr15) and Histone H3 phospho Ser10 (H3 pSer10) of proliferative (Prolif) and serum starved (Arrest) HeLa cells normalized by Vinculin. Mean and SD values are shown for $n = 3$ independent experiments; one sample t test, $** p = 0.0018$ and $ns p = 0.2335$ respectively.
- C. Schematic representation of experimental workflow.
- D. Sequencing tracks showing the mutations created on *WAPL* gene in HeLa cells. Since HeLa cells are triploid, mutations on the three alleles of *WAPL* gene are shown for clone 1 (lines 1-3) and clone 2 (lines 4-6). Mixed *WAPL* Δ cell populations displayed mutations on 100 % of the sequences screened (lines 7 onwards).
- E. Representative Gaussian renderings (multiple arbitrary colors) of clusters identified by cluster identification described in Ricci et al. (Ricci et al., 2015) of SMC1A in Control and *WAPL* Δ cells. SMC1A signal detected at the cytosol and nucleus in Control cells, vermicelli structures and SMC1A outside vermicelli have been segmented and analyzed separately. Lower panels display zoomed views of the nuclear regions indicated with white squares.
- F. Pearson correlation analysis of DNA-SMC1A and DNA-RNA Pol II phSer2 colocalization in 3-D confocal nuclei. Mean and SD values are plotted, $n = 14$ and 13 nuclei respectively; two-tailed unpaired t test, $**** p < 0.0001$.
- G. Dual-color super-resolution images of SMC1A (magenta) and RNA polymerase II phSer2 (RNAP II phSer2, green) in HeLa cells. Representative zoomed nuclear area is shown.
- H. Nearest Neighbor Distance (NND) distribution plot of the distance of RNAP II phSer2 clusters to SMC1A clusters and of SMC3 to SMC1A as positive control in HeLa cells; $n = 19$ and 30 nuclei respectively. SMC3-SMC1A dataset is also displayed in Figure S4B-E. Experimental data are shown as continuous lines, random simulated data are displayed as dotted lines.
- I. Nearest Neighbor Distance (NND) distribution between RNAP II phSer2 and SMC1A, and between SMC3 and SMC1A (positive control) clusters in HeLa cells. SMC3-SMC1A dataset is also displayed in Figure S4B-E. Values corresponding to the difference between experimental and random simulated data from panel H are plotted.

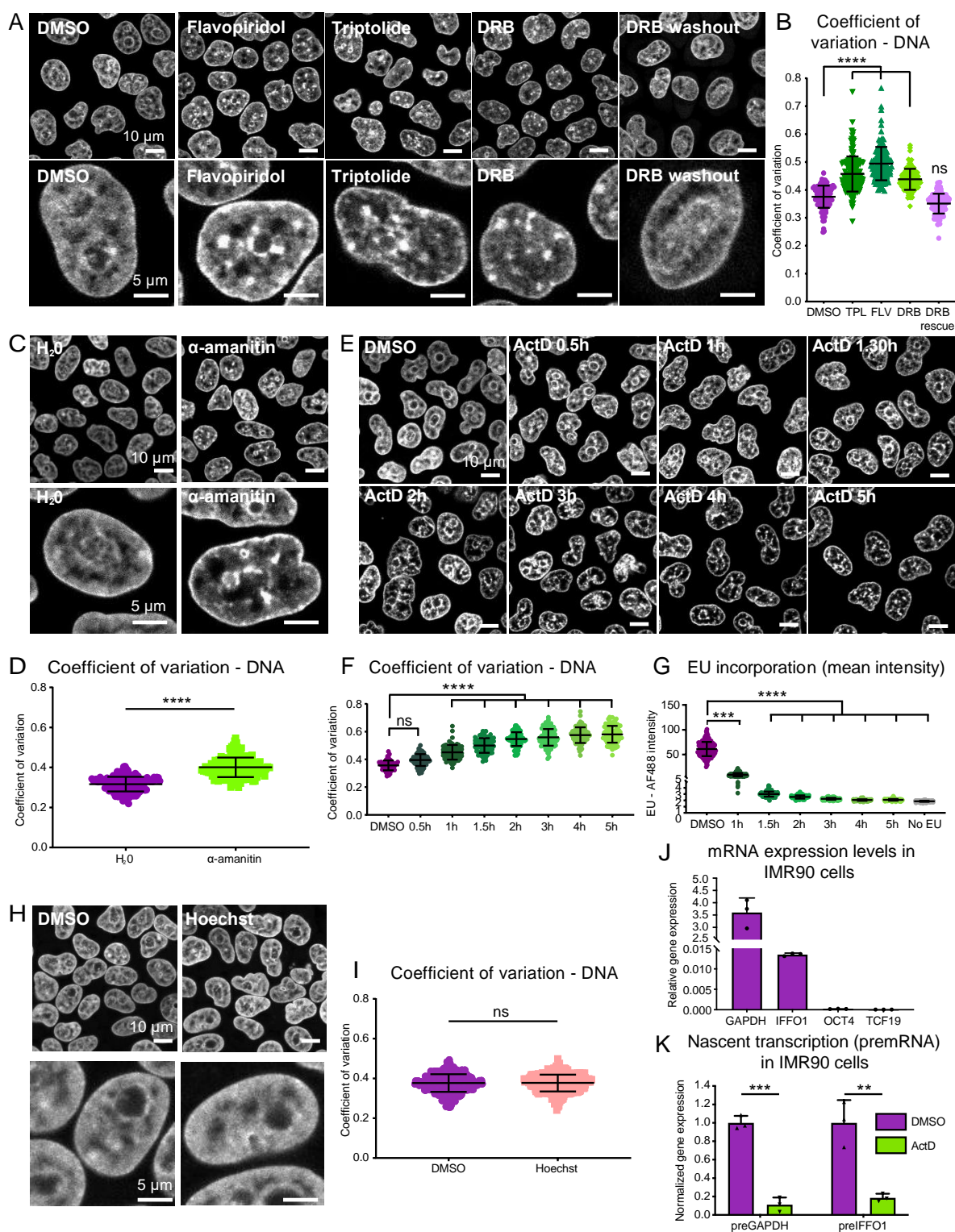


Figure S2. Inhibition of transcription causes specific and reversible DNA compaction, related to Figure 2

A. DAPI stained HeLa cells treated with DMSO as mock control, Triptolide, Flavopiridol and DRB for 5 h, and DRB followed by 24h washout (DRB

washout) as rescue control. Confocal stacks of representative images and zoomed individual nuclei are shown.

- B. Coefficient of variation of DAPI signal in HeLa cells treated with DMSO (mock control) Triptolide, Flavopiridol, DRB, and DRB followed by 24h washout (DRB washout). Confocal stacks were quantified in $n \geq 100$ nuclei. Mean and SD values are shown; Kruskal-Wallis test with Dunn's correction for multiple comparisons, **** $p < 0.0001$, ns $p = 0.1858$.
- C. DAPI stained HeLa cells treated with α -amanitin and H₂O as mock control for 7.5 h. Confocal stacks of representative images and zoomed individual nuclei are shown.
- D. Coefficient of variation of DAPI signal in HeLa cells treated with H₂O (mock control) and α -amanitin. Confocal stacks were quantified in $n \geq 150$ nuclei. Mean and SD values are shown; unpaired two-tailed t test, **** $p < 0.0001$.
- E. DAPI stained HeLa cells treated with ActD at multiple timepoints and DMSO as mock control. Confocal stacks of representative images are shown.
- F. Coefficient of variation of DAPI signal in HeLa cells treated with DMSO (mock control) and ActD at multiple timepoints (indicated in the plot). Confocal stacks were quantified in $n \geq 68$ nuclei. Mean and SD values are shown; Kruskal-Wallis test with Dunn's correction for multiple comparisons, **** $p < 0.0001$, ns $p = 0.5818$.
- G. Nuclear intensity quantification of Click-iT-AF488 stained HeLa cells treated with Actinomycin D at multiple timepoints (indicated in the plot) and DMSO in which EU has been incorporated the last hour of treatment to measure nascent RNAs. Confocal stacks were quantified in $n \geq 117$ nuclei. Mean and SD values are shown; Kruskal-Wallis test with Dunn's correction for multiple comparisons, *** $p = 0.0001$, **** $p < 0.0001$.
- H. DAPI stained HeLa cells treated with Hoechst and DMSO as mock control for 5h. Confocal stacks of representative images and zoomed individual nuclei are shown.
- I. Coefficient of variation of DAPI signal in HeLa cells treated with DMSO (mock control) and Hoechst. Confocal stacks were quantified in $n \geq 360$ nuclei. Mean and SD values are shown; unpaired two-tailed t test, ns $p = 0.9350$.
- J. qRT-PCR in IMR90 fibroblasts shows transcriptional expression of *GAPDH* and *IFFO1* and repression of *OCT4* and *TCF19* genes. dCt expression relative to *B-Actin*. Mean and SD values are shown for $n = 3$ independent experiments.
- K. qRT-PCR for nascent transcripts (unspliced pre-mRNA) shows transcriptional repression of *GAPDH* and *IFFO1* transcripts upon ActD treatment compared to DMSO controls. dCt expression relative to *B-Actin*

and normalized to DMSO controls. Mean and SD values are shown for n= 3 independent experiments; two-tailed unpaired t test, *** p = 0.0001, ** p = 0.0049.

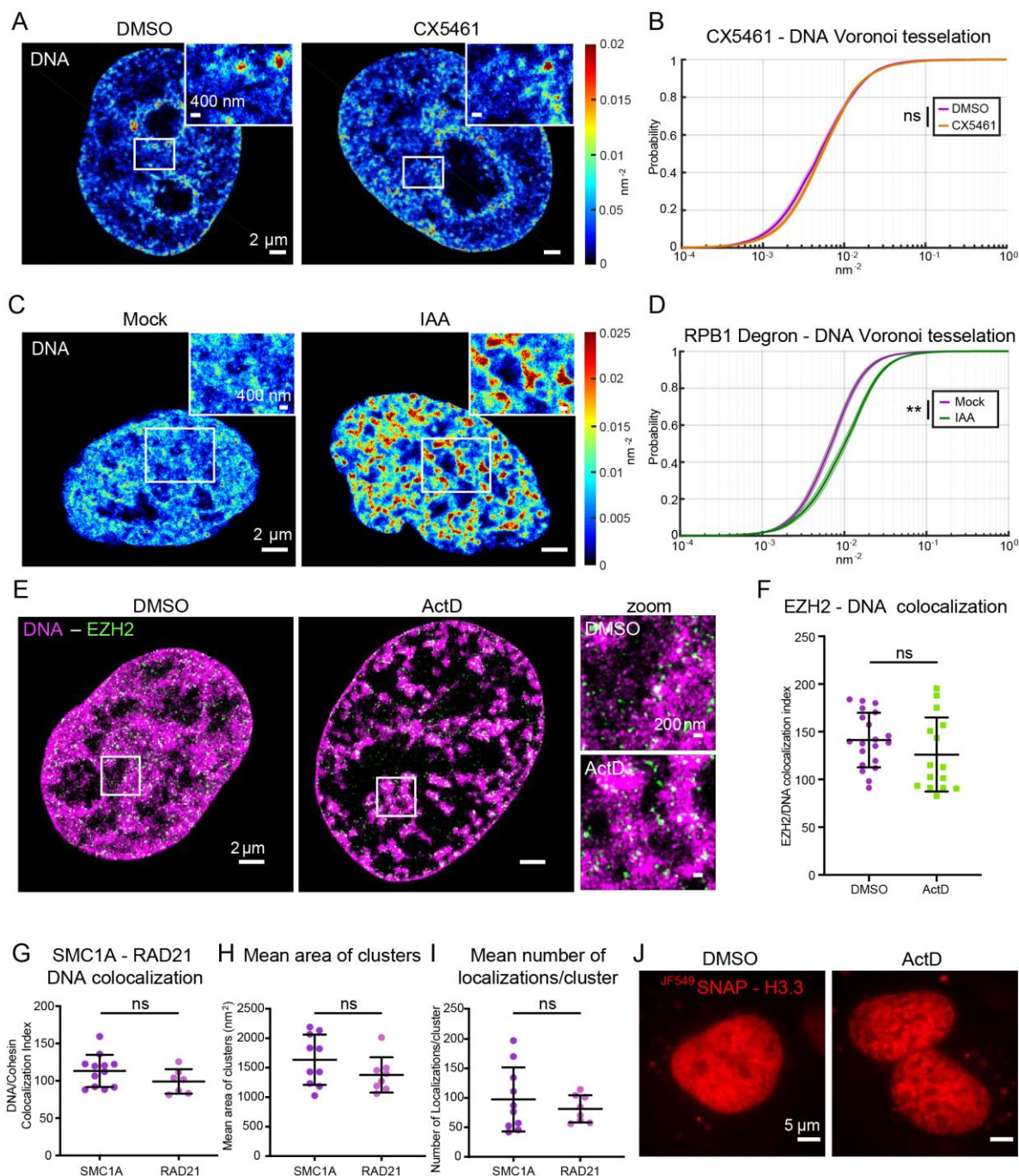


Figure S3. DNA compaction is specifically due to RNA polymerase II inhibition, related to Figure 3

- A. Heatmap density rendering of super-resolution images of DNA (EdC-AF647 labeling) in Control (DMSO) and CX5461 RNAP I inhibitor (CX5461) treated HeLa cells. Full nuclei and zoomed views (inset panels) are shown.
- B. Cumulative distribution of Voronoi polygons' densities of DNA in DMSO (purple, $n = 15$ nuclei) and CX5461-treated cells (ochre, $n = 12$ nuclei).

Median (thick line) and standard error of the mean values (SEM) (shaded area) are plotted; two-tailed Mann-Whitney test, ns $p = 0.4559$.

- C. Heatmap density rendering of super-resolution images of DNA (EdC-AF647 labeling) in Control (Mock) and 24h Indole Acetic Acid (IAA) treated mAID-mClover-RPB1 DLD1 cells. Full nuclei and zoomed views (inset panels) are shown.
- D. Cumulative distribution of Voronoi polygons' densities of DNA in Mock (violet, $n = 30$ nuclei) and 24h Indole Acetic Acid (IAA) treated (dark green, $n = 24$ nuclei) mAID-mClover-RPB1 DLD1 cells. Median (thick line) and standard error of the mean values (SEM) (shaded area) are plotted; two-tailed Mann-Whitney test, ** $p = 0.0017$.
- E. Super-resolution images of DNA (EdC-AF647 labeling, in magenta) and EZH2 (DNA-PAINT immunolabeling, in green) in Control (DMSO) and ActD-treated HeLa cells. Full nuclei (left panels) and zoomed views (right panels) are shown.
- F. Colocalization index of EZH2 with DNA in DMSO and ActD-treated cells ($n = 20$ and 15 nuclei respectively). Mean and SD are plotted; two-tailed unpaired t test, ns $p = 0.1891$.
- G. Colocalization index of SMC1A or RAD21 with DNA in HeLa cells ($n = 12$ and 7 nuclei respectively); SMC1A nuclei plotted here are also included among nuclei plotted in panel 3B. Mean and SD are plotted; two-tailed unpaired t test, ns $p = 0.1561$.
- H. Mean area of SMC1A and RAD21 clusters in HeLa cells ($n = 10$ and 8 nuclei respectively). Mean and SD are plotted; two-tailed unpaired t test, ns $p = 0.1702$.
- I. Mean number of localizations per cluster of SMC1A and RAD21 proteins in HeLa cells ($n = 10$ and 8 nuclei respectively). Mean and SD are plotted; two-tailed unpaired t test, ns $p = 0.4490$.
- J. Representative example SNAP-H3.3 RAD21-HaloTag U2OS cells labeled with JF549-SNAP ligand under DMSO and ActD-treated conditions. H3.3 labeling in living cells shows chromatin compaction upon ActD treatment.

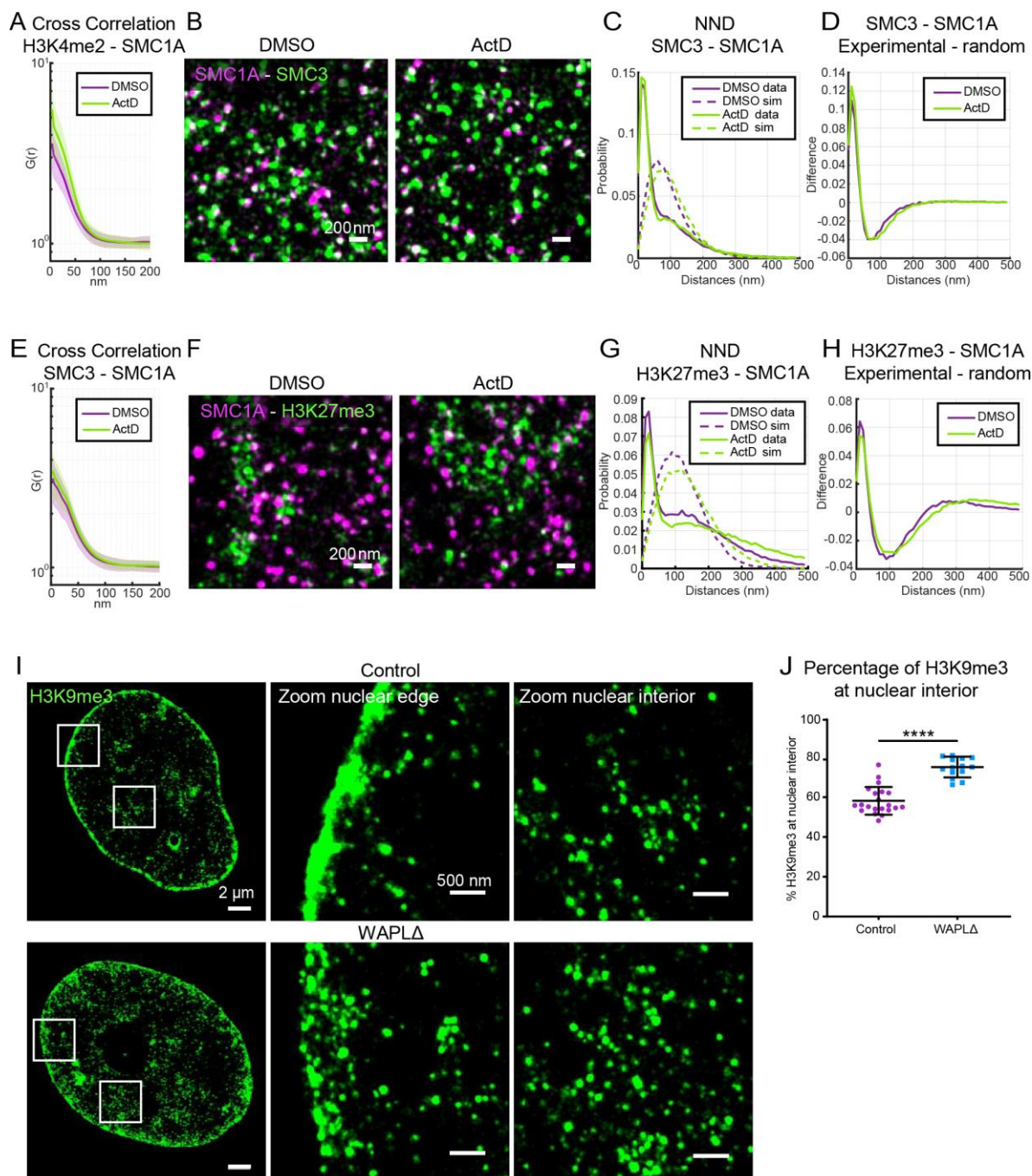


Figure S4. Inhibition of transcription does not affect SMC1A-SMC3 and SMC1A-H3K27me3 proximity, related to Figure 4

A. Cross pair correlation curves between H3K4me2 and SMC1A localizations in DMSO (purple) and ActD (green) HeLa cells. $N = 30$ and 23 nuclei respectively with 2-3 ROI analyzed per nucleus. Median (thick line) and SD (shaded area) values are plotted.

- B. Dual-color super-resolution images of SMC1A (magenta) and SMC3 (green) in DMSO and ActD HeLa cells. Representative zoomed nuclear areas are shown.
- C. Nearest Neighbor Distance (NND) distribution plot of the distance of SMC3 clusters to SMC1A clusters in DMSO and ActD HeLa cells; $n = 30$ and 25 nuclei respectively. DMSO dataset is also displayed in Figure S1H, I. Experimental data are shown as continuous lines, random simulated data are displayed as dotted lines.
- D. Nearest Neighbor Distance (NND) distribution between SMC3 and SMC1A clusters in DMSO (purple) and ActD (green) HeLa cells. DMSO dataset is also displayed in Figure S1H, I. Values corresponding to the difference between experimental and random simulated data from panel C are plotted.
- E. Cross pair correlation curves between SMC3 and SMC1A localizations in DMSO (purple) and ActD (green) HeLa cells; $n = 30$ and 24 nuclei respectively with 2-3 ROI analyzed per nucleus. Median (thick line) and SD (shaded area) values are plotted.
- F. Dual-color super-resolution images of SMC1A (magenta) and H3K27me3 (green) in DMSO and ActD HeLa cells. Representative zoomed nuclear areas are shown.
- G. Nearest Neighbor Distance (NND) distribution plot of the distance of H3K27me3 clusters to SMC1A clusters in DMSO and ActD HeLa cells; $n = 13$ nuclei each. Experimental data are shown as continuous lines, random simulated data are displayed as dotted lines.
- H. Nearest Neighbor Distance (NND) distribution between H3K27me3 and SMC1A clusters in DMSO (purple) and ActD (green) HeLa cells. Values corresponding to the difference between experimental and random simulated data from panel G are plotted.
- I. Super-resolution images of H3K9me3 (green) in Controls and WAPL Δ cells. Right panels display zoom in views of the nuclear regions indicated with white squares.
- J. Percentage of H3K9me3 at nuclear interior quantified in Controls and WAPL Δ ($n = 21$ and 14 nuclei respectively). Mean and SD values are plotted; unpaired two-tailed t test, **** $p < 0.0001$.

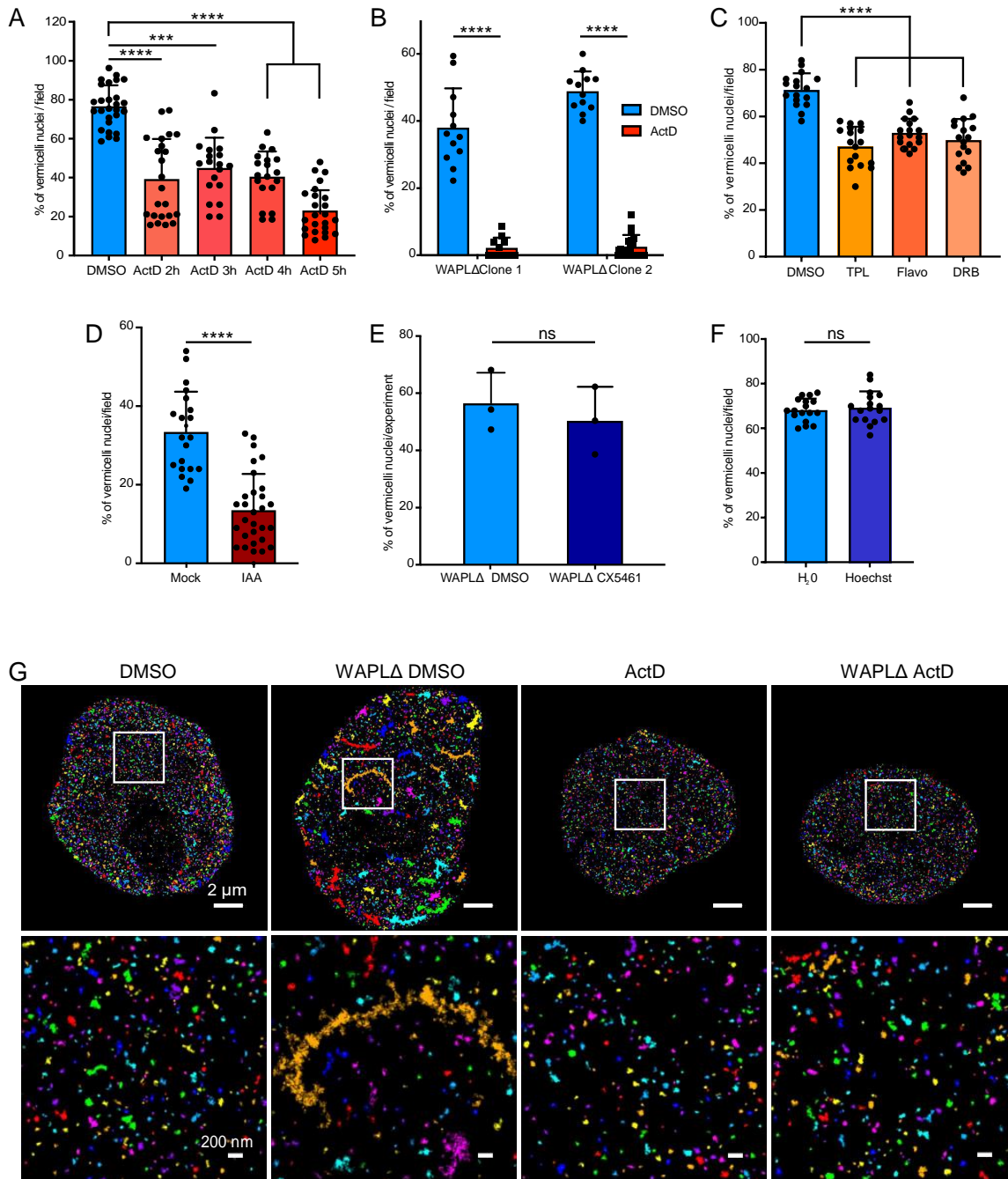


Figure S5. Inhibition of RNAP II specifically abrogates the formation of vermicelli in WAPLΔ cells, related to Figure 5

A. Percentage of cells with vermicelli per field in DMSO and ActD-treated at multiple timepoints in WAPLΔ cell populations, $n \geq 19$ fields. Mean and SD are plotted; Kruskal-Wallis test with Dunn's correction for multiple comparisons, *** $p = 0.0002$, **** $p < 0.0001$.

- B. Percentage of cells with vermicelli per field in DMSO and ActD-treated WAPLΔ clones, $n \geq 11$ fields. Mean and SD are plotted; two-tailed Mann-Whitney test, **** $p < 0.0001$.
- C. Percentage of cells with vermicelli per field in DMSO as mock control, Triptolide, Flavopiridol and DRB for 5 h treated WAPLΔ cell populations, $n = 17$ fields. Mean and SD are plotted; two-tailed Mann-Whitney test, **** $p < 0.0001$.
- D. Percentage of cells with vermicelli per field in Mock and IAA-treated WAPLΔ cell populations, for IAA treated cells, % vermicelli nuclei among mClover negative cells (RNAP II degraded) is shown, $n \geq 21$ fields. Mean and SD are plotted; two-tailed Mann-Whitney test, **** $p < 0.0001$.
- E. Percentage of cells with vermicelli per experiment in DMSO and CX5461-treated WAPLΔ cell populations, $n = 3$ independent experiments. Mean and SD are plotted; two-tailed Mann-Whitney test, ns $p = 0.700$.
- F. Percentage of cells with vermicelli per field in H₂O and Hoechst-treated WAPLΔ cell populations, $n = 17$ fields. Mean and SD are plotted; two-tailed Mann-Whitney test, ns $p = 0.6762$.
- G. Representative Gaussian renderings (multiple arbitrary colors) of clusters identified by Voronoi tessellation analysis of SMC1A in DMSO, WAPLΔ DMSO, ActD and WAPLΔ ActD cells. Lower panels display zoomed views of the nuclear regions indicated with white squares.

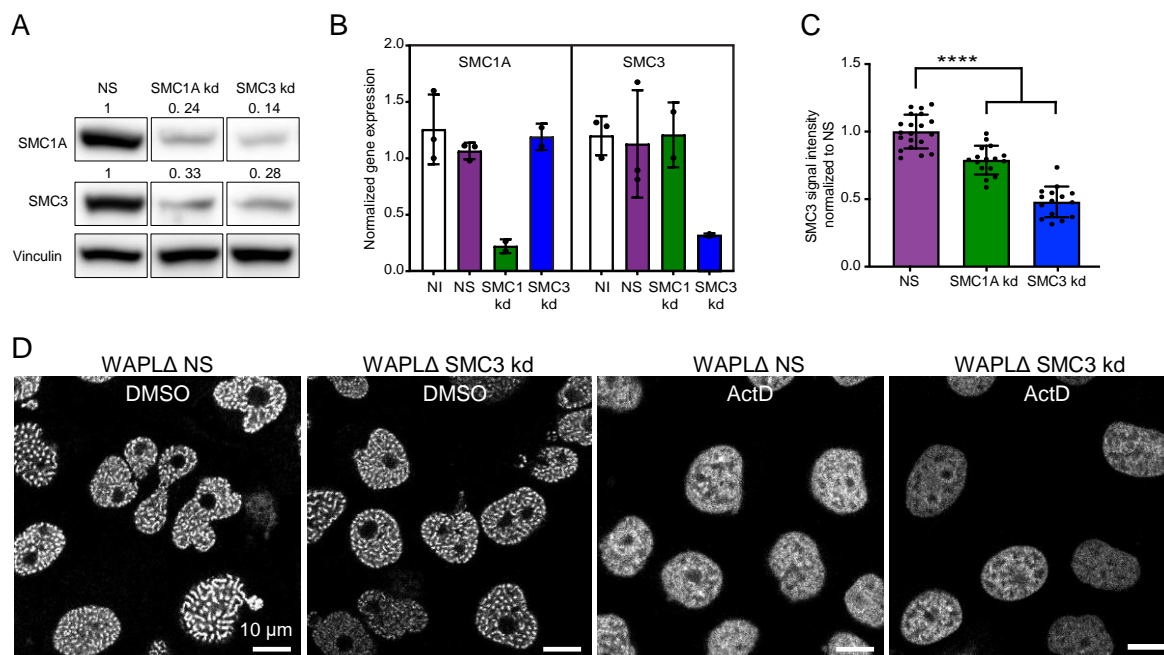


Figure S6. Cohesin knockdown does not abrogates the formation of vermicelli in WAPLΔ cells, related to Figure 5

- Representative Western Blots for total protein extracts of Control non-silencing shRNA (NS), *SMC1A* and *SMC3* knockdown (kd) HeLa cells. *SMC1A*, *SMC3* and vinculin blots are shown. Densitometric quantification of blots is shown above each band normalized by NS; reduction of protein signal of 76 and 74 % for *SMC1A* kd and *SMC3* kd, respectively.
- qPCR for *SMC1A* and *SMC3* expression in non-infected (NI), non-silencing control shRNA (NS), *SMC1A* kd and *SMC3* kd HeLa cells. dCt expression relative to *GAPDH* and normalized to NS controls. Reduction of RNA signal of 78 and 68 % for *SMC1A* kd and *SMC3* kd respectively; mean and SD values are shown for $n \geq 2$ independent experiments.
- Quantification of *SMC3* fluorescence intensity in Control shRNA (NS), *SMC1A* kd and *SMC3* kd HeLa cells. $n \geq 15$ nuclei; one-way ANOVA with Tukey's test for multiple comparisons, **** $p < 0.0001$.
- Representative confocal images for *SMC3* in WAPLΔ NS control and WAPLΔ *SMC3* kd, DMSO and ActD-treated HeLa cells.

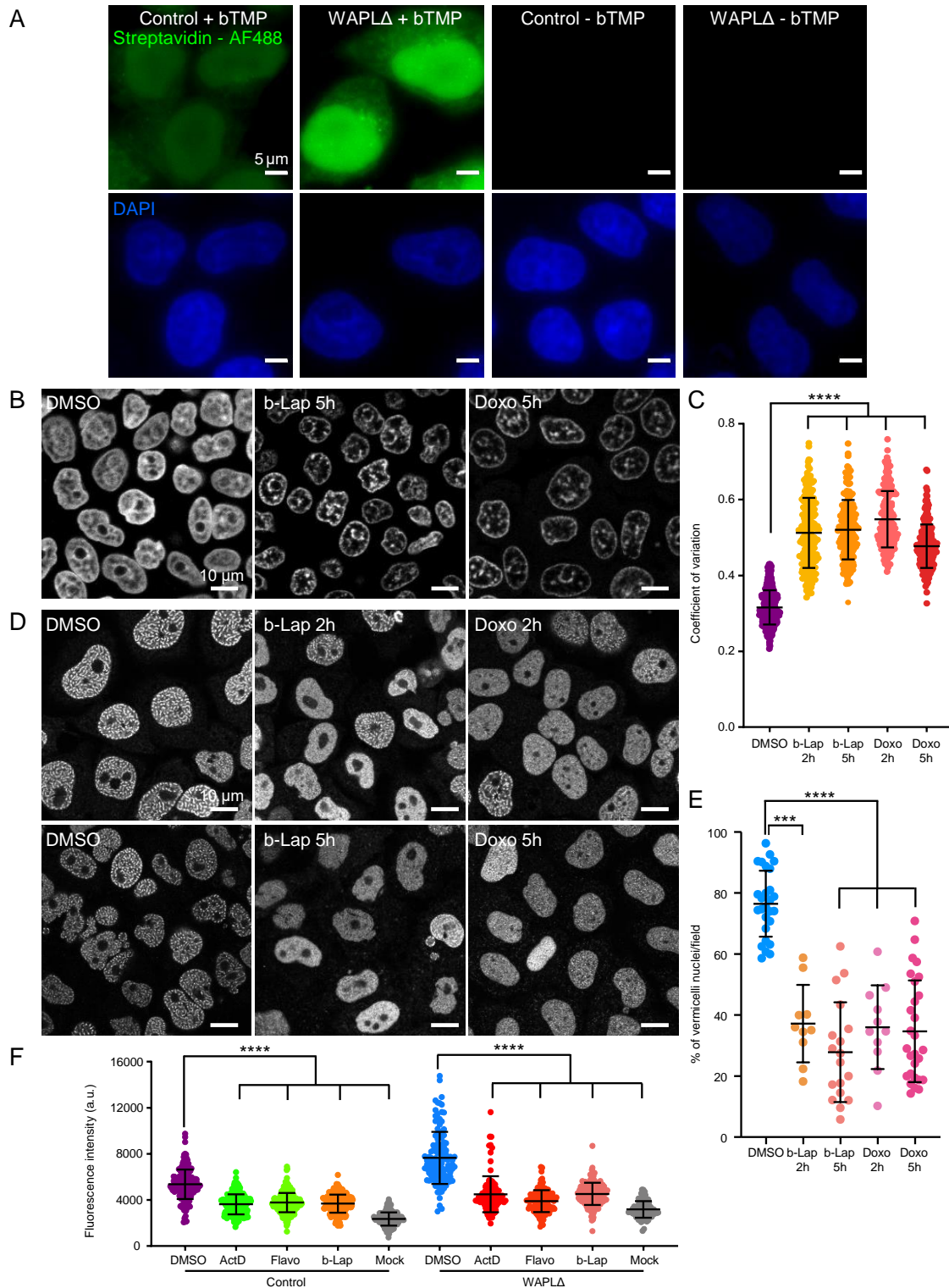


Figure S7. Topoisomerase inhibition leads to DNA compaction, reduced level of negative supercoiling and loss of vermicelli formation, related to Figure 6

A. Representative images of control and WAPL Δ HeLa cells incubated with bTMP or mock controls (-bTMP) and stained with AF488 conjugated Streptavidin. DNA was stained with DAPI.

- B. DAPI stained HeLa cells treated with DMSO, b-lapachone (b-Lap) and Doxorubicin (Doxo), 5 h treatments. Confocal stacks of representative images are shown.
- C. Coefficient of variation of DAPI signal in HeLa cells treated with DMSO, b-Lap and Doxo, 2 and 5 h treatments. Confocal stacks were quantified in $n \geq 187$ nuclei. Mean and SD values are plotted; Kruskal-Wallis test with Dunn's correction for multiple comparisons, **** $p < 0.0001$.
- D. Representative confocal images for SMC1A in DMSO, b-Lap- and Doxo-treated WAPLΔ HeLa cells (2 and 5 h treatments).
- E. Percentage of cells with vermicelli per field in DMSO and b-Lap- and Doxo-treated WAPLΔ cell populations (2 and 5 h treatments), $n \geq 10$ fields. Mean and SD are plotted; Kruskal-Wallis test with Dunn's correction for multiple comparisons, *** $p = 0.0003$, **** $p < 0.0001$.
- F. Mean Fluorescence intensity in arbitrary units (Neutravidin-OG488) of bTMP treated control and WAPLΔ cells, treated with DMSO, ActD, Flavopiridol (Flavo), b-Lap and Doxo and of mock controls (-bTMP) of both cell types. Mean and SD, $n \geq 85$ nuclei; Kruskal-Wallis test with Dunn's correction for multiple comparisons, **** $p < 0.0001$.

SUPPLEMENTAL TABLES and LEGENDS

| Genomic enrichment H3K4me2 ChIP-seq peaks at active TSS in HeLa cells | | |
|---|---|-------------------------------------|
| Number of active TSS (> 2 tpm) | Number of active TSS with ≥ 1 H3K4me2 peak | % of TSS with ≥ 1 H3K4me2 peak |
| 37952 | 27136 | 71.5 % |

| Genomic distribution of H3K4me2 ChIP-seq peaks in HeLa cells | |
|--|--------------|
| Genomic elements | % of H3K4me2 |
| Promoter | 19.59 |
| 5' UTR | 0.38 |
| 3' UTR | 1.84 |
| First exon | 1.62 |
| Other exons | 2.32 |
| First intron | 30.72 |
| Other introns | 23.25 |
| Downstream (≤ 300 bp) | 1.03 |
| Distal intergenic | 19.25 |

Table S1. Genomic distribution of H3K4me2 ChIP-seq peaks in HeLa cells, related to Figure 3.

Upper part: Enrichment of H3K4me2 across active Transcription Start Sites (TSS). Coordinates of active TSS were obtained from our RNA-seq dataset considering genes having an average detected expression > 2 TPM. Number of active TSS with ≥ 1 H3K4me2 peak was obtained by overlapping active TSS with H3K4me2 ChIP-seq peaks.

Lower part: H3K4me2 ChIP-seq peaks were annotated and classified using the ChIPseeker tool (Yu et al., 2015).

| Fisher's Exact Test | |
|---------------------|----------|
| Cell type | p value |
| GM12878 | 4.19E-17 |
| HeLa | 4.51E-22 |
| NHEK | 5.25E-23 |
| HUVEC | 8.41E-09 |
| IMR90 | 2.94E-17 |
| K562 | 1.27E-32 |
| H1 | 6.96E-55 |

Table S2. Enrichment of expressed genes within loop domains, related to Figure 5. p values for Fisher Exact Test are reported, showing statistically significant enrichment of expressed genes within loop domains across seven cell types. Loop domain coordinates were obtained from Rao et al., 2014 Hi-C datasets for GM12878, HeLa, NHEK, HUVEC, IMR90, K562 cells and from Krietenstein et al., 2020 Micro-C dataset for H1 cells.

| | Percentage (%) of loops with expressed genes in: | | | | | | |
|---------------------|--|-------|-------|-------|-------|-------|-------|
| Level of expression | GM12878 | HeLa | NHEK | HUVEC | H1 | IMR90 | K562 |
| Above threshold | 83.13 | 85.84 | 79.49 | 87.74 | 70.57 | 83.69 | 85.57 |
| Top 75 % | 75.01 | 78.99 | 69.95 | 81.03 | 63.38 | 77.35 | 77.12 |
| Top 50 % | 63.09 | 66.39 | 55.69 | 70.35 | 52.80 | 65.21 | 64.55 |
| Top 25 % | 39.66 | 40.43 | 32.16 | 42.98 | 33.26 | 38.79 | 40.65 |

Table S3. Percentage of loop domains containing expressed genes, related to Figure 5.

Genes were classified based on their level of gene expression for every given cell type, expression levels were classified in percentiles (RNA-seq data from Gencode). Loop domain coordinates were obtained from Hi-C datasets (Rao et al., 2014) for GM12878, HeLa, NHEK, HUVEC, IMR90, K562 cells and from Micro-C (Krietenstein et al., 2020) dataset for H1 cells.

| Drug | Concentration | Solvent | Brand – Code |
|----------------------|----------------------|------------------|----------------------------|
| Actinomycin D (ActD) | 4 μ M | DMSO | Sigma-Aldrich, #A9415 |
| DRB | 100 μ M | DMSO | Sigma-Aldrich, #D1916 |
| Flavopiridol | 10 μ M | DMSO | Sigma-Aldrich, #F3055 |
| Triptolide | 200 nM | DMSO | Tocris, #3253 |
| α -amanitin | 50 μ g/ml | H ₂ O | Sigma-Aldrich, #A2263 |
| Hoechst | 5 μ g/ml | DMSO | Thermofisher, #H1399 |
| CX-5461 | 1 μ M | DMSO | Sigma-Aldrich, #5092650001 |
| b-lapachone | 10 μ M | DMSO | Sigma-Aldrich, #L2037 |
| Doxorubicin | 5 μ M | DMSO | Sigma-Aldrich, #324380 |
| Doxycycline | 1 μ g/ml | DMSO | Sigma-Aldrich, #D9891 |
| IAA | 500 μ M | DMSO | Sigma-Aldrich, #I5148 |

Table S4. List of drugs used to inhibit transcription and topoisomerases, related to Star Methods

| Region/Name | Forward | Reverse | Application |
|--------------------|---------------------------------------|--|---|
| GAPDH- IFFO1 | CAAGGAGCC GTCGAGGCA AG | GGTCGGGTTTGGCGA GGAAC | Quality check / Library amplification |
| OCT4-TCF19 | GATACGCGA GCTCACGCC AG | CGCACGCATAGCGTC TACCG | |
| GAPDH- IFFO1 | CAAGGAGCC GTCGAGGCA AG | TAATACGACTCACTAT AGGGTCGGGTTTGGC GAGGAAC | T7 touch up PCR |
| OCT4-TCF19 | GATACGCGA GCTCACGCC AG | TAATACGACTCACTAT AGCGCACGCATAGCG TCTACCG | T7 touch up PCR |
| GAPDH- IFFO1 | /5AF405N/GGA GGACGAGGC GTCTACCG | | RT |
| OCT4-TCF19 | /5AF405N/GAG GAAGCGTAC CAGCACGG | | RT |
| GAPDH- IFFO1 | CGGTAGACG CCTCGTCCTC C/3AF647N/ | | OligoSTORM secondary probe |
| OCT4-TCF19 | CCGTGCTGG TACGCTTCCT C/3AF647N/ | | OligoSTORM secondary probe |

Table S5. Primers and sequences used for Oligopaint synthesis and detection, related to Star Methods.

| Gene | Forward primer | Reverse primer |
|------------------|----------------------------|------------------------------|
| β -ACTIN | ATAGCAACGTACATGGCTG G | CACCTTCTACAATGAGCTGC |
| GAPDH | AGCCACATCGCTCAGACAC | GCCCAATACGACCAAATCC |
| premRNA GAPDH | CCCATCCCTTCTCCCCACA C | CCCCTAGTCCCAGGGCTTTG |
| IFFO1 | GACGTGCAGATGGAGACCT G | CGCAGTGAAAGCAGGAGACT T |
| premRNA IFFO1 | CAGAATCAATGGCACCTCC A | AAAGGGGCCCAATCCTCTTA |
| OCT4 | GCTGGAGCAAAACCCGGA GG | TCGGCCTGTGTATATCCCAGG GTG |
| TCF19 | CCACTGGAAATCGACGTGG C | GCAACAAGGAGCTGCACAGG |
| SMC1A | ACCCAATGGCTCTGGTAAG TCA | CCCGCAGGTTGCTGGTTTTT |
| SMC3 | CCAGATGGCAACAGCACCA G | TCCCGTTTGCCCTCTGTTTC |

Table S6. List of oligos used for qPCR, related to Star Methods.